

UNIVERSITY OF SÃO PAULO  
FFCLRP – DEPARTMENT OF PHYSICS  
Postgraduate in Applied Physics to Medicine and Biology

SAEIDEH ARSALANI

**Evaluation of magnetic nanoparticle as magneto-  
motive ultrasound imaging contrast**

**Avaliação de nanopartículas magnéticas no  
contraste magneto-acustografia**

Ribeirão Preto – SP

2018

SAEIDEH ARSALANI

**Evaluation of magnetic nanoparticle as magneto-  
motive ultrasound imaging contrast**

**Avaliação de nanopartículas magnéticas no  
contraste magneto-acustografia**

Dissertation presented to Faculty of Philosophy, Sciences and Literature of the University of São Paulo, as part of the requirements for acquirement the grade of Master of Sciences.

**Concentration area:** Applied Physics to Medicine and Biology.

**Advisor:** Prof. Dr. Antonio Adilton Oliveira Carneiro

Ribeirão Preto – SP  
2018

I authorize partial and total reproduction of this work, by any conventional or electronic means, for the purpose of study and research, provided the source is cited.

## FICHA CATALOGRÁFICA

Serviço de Documentação da Universidade de São Paulo  
Faculdade de Filosofia, Ciências e Letras de Ribeirão Preto

Saeideh Arsalani

Evaluation of magnetic nanoparticle as magneto-motive ultrasound imaging contrast / Saeideh arsalani; Orientador: Prof. Dr. Antonio Adilton Oliveira Carneiro.

Ribeirão Preto - SP, 2018.

74 f.:il.

Dissertation (M.Sc. - Postgraduate Program in Applied Physics to Medicine and Biology) - Faculty of Philosophy, Sciences and Literature of the University of São Paulo, 2018.

1. Ultrasound. 2. Magnetic nanoparticles. 3. Elastography. 4. Shear wave. 5. Magneto motive ultrasound. 6. Viscoelasticity properties. 7. Tissue mimicking phantom.

Name: Saeideh Arsalani

Title: Evaluation of magnetic nanoparticle as magneto-motive ultrasound imaging contrast  
Avaliação de nanopartículas magnéticas no contraste magneto-acustografia

Dissertation presented to Faculty of Philosophy,  
Sciences and Literature of the University of São  
Paulo, as part of the requirements for acquirement  
the grade of Master of Sciences.

Approved in:

Examination Board

Prof. Dr. \_\_\_\_\_

Institution: \_\_\_\_\_

Judgment: \_\_\_\_\_

Prof. Dr. \_\_\_\_\_

Institution: \_\_\_\_\_

Judgment: \_\_\_\_\_

Prof. Dr. \_\_\_\_\_

Institution: \_\_\_\_\_

Judgment: \_\_\_\_\_

I dedicate this work to my beloved father.

---

# ACKNOWLEDGMENTS

---

First of all, I would like to thank God because of helping me in all aspects of my life.

I would like to express my deep gratitude to my advisor, Dr. Antonio Adilton Oliveira Carneiro for his valuable advice, guidance and endless inspiration during my project. He has been an invaluable mentor, who helped me in doing a lot of research and I learnt a lot working with him, I am really thankful to him.

My special and sincere thanks to my best colleague, Yaser Hadadian, for his untiring supports and suggestions whenever I need his help. I would like to mention about our countless talk and discussion related to my project.

Many thanks to another colleague, Diego Sampaio for being always helpful and suggesting great ideas. Moreover, I am also thankful to the other colleagues Luciana, Felipe and Guilherme to make me feel welcome and for providing a good environment during these two years.

Moreover, I would like to thank to Dr. Theo Pavan and Oswaldo Baffa Filho for all their supports and kindness.

Also, I also thank to our technician in GIIMUS, Agnelo Bastos, for all his guidance and patience during my experiments.

I am also thankful from Nilza and Ricardo for all necessary information and suggestions have given for doing the process of my defense.

Furthermore, I am grateful to my friends such as Alejandro, Iara, Kleython, Mehran, Leo, David and Ignacio for their encouragement, understanding, and patience even during hard times of this studies. Also, they have provided me with great memories.

Lastly, I would like to thank my family for their unconditional support, love and encouragement, not only with my education but in all aspects of my life. Many thanks to all my sisters and my brother for always being by my side and believing in me. Especially my sister, Sudi, for her caring and kindness as well as kept me motivated to do always the best I could. I couldn't have done it without them.

Saeideh Arsalani

---

# RESUMO

---

Saeideh Arsalani. **Avaliação de nanopartículas magnéticas no contraste ultrassonográfica magnetomotriz.** 2018. 83 f. Dissertação (Mestrado – Programa de Pós-Graduação em Física Aplicada à Medicina e Biologia) - Departamento de Física da Faculdade de Filosofia, Ciências e Letras de Ribeirão Preto, Universidade de São Paulo, Ribeirão Preto; 2018.

Nanopartículas magnéticas têm sido comprovadas como material promissor para uso em biologia e medicina, incluindo purificação de proteínas, detecção de bactérias, liberação de drogas, hipertermia e técnicas de imagem, como ressonância magnética (MRI), tomografia por emissão de posição (PET), emissão de fóton único tomografia computadorizada (SPECT) e imagem óptica.

Recentemente, vários pesquisadores têm desenvolvido imagens de ultrassom magnetomotriz (MMUS) como técnica de imagem para melhorar a sensibilidade do ultrassom quando a nanopartículas magnéticas como contraste. Nesta técnica (MMUS), uma excitação magnética externa é aplicada a fim de induzir movimento dentro do tecido marcado com nanopartículas magnéticas e as ondas ultrassônicas (ondas RF) retroespalhadas são usadas para localizar e visualizar os movimentos induzidos. Essas vibrações, na ordem de micrometros, são originadas da interação das nanopartículas com um campo magnético oscilante externo. Recentemente, uma subdivisão da MMUS, denominada de ultrassom magnetomotriz por dispersão de ondas de cisalhamento (SDMMUS), tem sido desenvolvida como uma nova técnica de elastografia remota para analisar as propriedades mecânicas do meio. A interação das nanopartículas magnéticas com um campo magnético gera uma onda de cisalhamento e a propagação dessa onda fornece informações sobre as propriedades de viscoelasticidade do meio, incluindo a elasticidade de cisalhamento ( $\mu_1$ ) e a viscosidade de cisalhamento ( $\mu_2$ ). Neste método, o algoritmo de Levenberg-Marquardt, como ajuste não-linear, foi aplicado para calcular a velocidade da onda de cisalhamento versus a frequência de excitação, para estimar os parâmetros de viscoelasticidade.

Nesta tese, vários tecidos sintéticos (simuladores) a base gelatina que mimetizam o tecido biológico mole, marcados com nanopartículas superparamagnéticas ( $\text{Fe}_3\text{O}_4$ ) com diferentes magnetizações de saturação foram avaliados como contraste ultrassônico. Em cada um dos

simuladores foi usada uma inclusão marcada com nanopartículas magnéticas para gerar imagens de ultrassom SDMMUS. O efeito da magnetização de saturação (que está diretamente relacionada à suscetibilidade magnética das nanopartículas) em experimentos SDMMUS foi investigado e as propriedades mecânicas dos simuladores, incluindo a elasticidade de cisalhamento e a viscosidade de cisalhamento, foram calculadas a partir das ondas de cisalhamento geradas. Finalmente, de acordo com os resultados, a melhor nanopartícula magnética, entre as que foram usadas nesta tese, foi a de  $\text{Fe}_3\text{O}_4$  coberta com látex. Como era de se esperar, essa nanopartícula otimizada foi a que apresentou a maior saturação magnética e os resultados confirmaram a proporção linear de magnetização de saturação com o deslocamento das estruturas internas dos simuladores, induzido pela magnetização das próprias nanopartículas.

**Palavras Chave:** 1. Ultrassom. 2. Nanopartículas magnéticas. 3. Elastografia. 4. Ondas transversais. 5. Ultrassom magnetomotriz. 6. Propriedades viscoelásticas. 7. Simulador de gelatina

---

# ABSTRACT

---

Saeideh Arsalani. **Evaluation of magnetic nanoparticle as magneto-motive ultrasound imaging contrast.** 2018. 83 f. Dissertation (M.Sc. - Postgraduate Program in Applied Physics to Medicine and Biology) - Faculty of Philosophy, Sciences and Literature, University of São Paulo, Ribeirão Preto - SP, 2018.

Magnetic nanoparticles have been proven as great promising material for biology and medicine applications including protein purification, bacterial detection, drug delivery, hyperthermia and imaging techniques such as magnetic resonance imaging (MRI), position emission tomography (PET), single photon emission computed tomography (SPECT), optical imaging and magnetic particle imaging.

Recently several researchers have been developing magnetomotive ultrasound imaging (MMUS) as an imaging technique to improve the sensitivity of ultrasound to detect magnetic nanoparticles. In this technique (MMUS), an external magnetic excitation is applied in order to induce a motion within tissue labeled with magnetic nanoparticles and the backscattered ultrasound radio frequency (RF) waves are used to localize and image the magnetically induced motions within tissue. These vibrations, in order of micro meters, are originated from the interaction of the particles with an external oscillating magnetic field. Lately, a type of MMUS, shear-wave dispersion magneto-motive ultrasound (SDMMUS) has been proposed to analyze the mechanical properties of the medium as a remote elastography novel technique. Interaction of the magnetic nanoparticles with an external magnetic field can generate a shear wave within the medium which has been labeled with these nanoparticles. The propagation of this wave provides information about viscoelastic properties of the medium including shear elasticity ( $\mu_1$ ) and shear viscosity ( $\mu_2$ ). In this method, the Levenberg–Marquardt algorithm, as a nonlinear fitting, was applied to calculate the velocity of shear wave versus excitation frequency in order to estimate viscoelasticity parameters.

In this thesis, various tissue mimicking phantoms of gelatin, labeled with different superparamagnetic nanoparticles ( $\text{Fe}_3\text{O}_4$ ) with different magnetization, were evaluated as ultrasound contrast. For each phantom one inclusion was used to generate shear wave dispersion magneto motive ultrasound imaging (SDMMUS). The effect of magnetization (which is directly related to magnetic susceptibility) on SDMMUS experiments were

investigated and mechanical properties of the phantoms including shear elasticity and shear viscosity were calculated using generated shear wave. Finally, according to the results the optimized magnetic nanoparticle among those which were used in this thesis was  $\text{Fe}_3\text{O}_4$  covered with latex. As it was expected, this optimized nanoparticle was the one with the highest magnetization and the results confirmed the direct relation of magnetization with induced displacement of magnetic nanoparticles.

**Keywords:** 1. Ultrasound. 2. Magnetic nanoparticles. 3. Elastography. 4. Shear wave.  
5. Magnetomotive ultrasound. 6. Viscoelasticity properties. 7. Tissue mimicking phantom.

---

# LIST OF FIGURES

---

Figure 1.1: Longitudinal wave (a) and shear wave (b).....	4
Figure 1.2: Strain – stress relationship for an ideal elastic matter (left). Illustrating hysteresis, strain - stress relationship for a viscoelastic matter (right).....	6
Figure 1.3: A schematic of Kelvin-Voigt model.....	7
Figure 1.4: The behavior of magnetic material in exposure of an external magnetic field.....	13
Figure 2.1: Figure 2.1: Image of the experimental system (a-c). A ferrite core is included in the center of a coil to enhance and focus the magnetic field gradient (c).....	21
Figure 2.2: Schematic depiction of the experimental setup used to perform the measurements.....	22
Figure 2.3: The rotation system to homogenize the phantom .....	26
Figure 2.4: Mimicking phantom with: (a) spherical and (b) cylindrical inclusion shape.....	26
Figure 2.5: The cylindrical phantom that a spherical inclusion is embedded in.....	27
Figure 2.6: MMUS platform user interface.....	28
Figure 2.7: The user interfaces of an MMUS timing sequence. (a) Ultrasound acquisition and (b) Magnetic excitation.....	29
Figure 2.8: 2-D particle velocity map [101] .....	31
Figure 2.9: Figure 2.9: The MMUS graphical user interface used to obtain 1) B-mode image; 2) MMUS image; 3) Power spectrum of the displacement.....	31
Figure 2.10: Analysis of shear wave signal. (a) Displacement image, (b) region of interest selected to obtain a spatial average of the particle displacement signal, (c) the average particle displacement signal and its (d) frequency spectrum.....	32
Figure 2.11: The shear wave analysis is performed via the window of analysis of MMUS platform, it shows three shear wave signals at 51, 46, and 41 depths.....	33
Figure 2.12: The time to peak algorithm is used to obtain shear wave peak position as a function of time, and then a linear fitting is applied obtain the shear wave velocity.....	34
Figure 3.1: The profile of the magnetic field respect to the tip of the coil. a) Oscillating magnetic field 3 mm far from the tip; b) Amplitude the magnetic field for different distance from tip.....	35

Figure 3.2: Propagation of the shear wave in the phantom with 4% of gelatin and 4% of nanoparticle with magnetic excitation of 50Hz in two different times (18.5 and 30 ms) .....	37
Figure 3.3: Displacement of the shear wave through the phantom for 4% gelatin and 4% concentration of Fe <sub>3</sub> O <sub>4</sub> in three depths.....	37
Figure 3.4: Frequency of the magnetic nanoparticles movement.....	37
Figure 3.5: Propagation of the shear wave in the phantom with 4% of gelatin and 0.5% of nanoparticle .....	38
Figure 3.6: The frequency of the magnetic nanoparticles movement (0.5% concentration of Fe <sub>3</sub> O <sub>4</sub> ).....	38
Figure 3.7: Propagation of the shear wave in the phantom with 4% of gelatin and 1% of nanoparticle as an inclusion in .....	39
Figure 3.8: Displacement of the shear wave by the gelatin phantom (4%) and 1% concentration of Fe <sub>3</sub> O <sub>4</sub> (a) and frequency of the magnetic nanoparticles movement (b).....	39
Figure 3.9: Magnetization curves for sample 2 (14 nm) and sample 3 (20 nm) .....	40
Figure 3.10: Propagation of the shear wave in the phantom with 4% of gelatin and 1% of nanoparticle (sample 2: 14 nm) as an inclusion .....	40
Figure 3.11: Propagation of the shear wave in the gelatin phantom (4%) and 1% of nanoparticles (sample 3, 20 nm) as an inclusion.....	41
Figure 3.12: Displacement of the shear wave by the phantom for 4% of gelatin and 1% concentration of the sample 2 (a) and sample 3 (b).....	41
Figure 3.13: The frequency of the magnetic nanoparticles movement for sample 2 (a) and 3 (b) respectively.....	41
Figure 3.14: Velocities of shear wave versus different frequencies (sample 2 and 3).....	42
Figure 3.15: TEM images and histograms of the particle size distribution of bare MNPs (a-b) and for 100NRL (c-d) and 800NRL (e-f).....	43
Figure 3.16: Magnetization curves of MNPs and NRL-coated MNPs measured by Hall magnetometer considering only the mass of iron oxide nanoparticles (MNPs).....	44
Figure 3.17: Propagation of the shear wave in the phantom with 4% of gelatin and 1% (a) and 0.3% (b) of nanoparticles (MNPs) inclusion.....	44
Figure 3.18: Displacement of the shear wave by the phantom (4% gelatin) and 1 % concentration (a ) and 0.3% of MNPs (b).....	45
Figure 3.19: The frequency of the magnetic nanoparticles movement for 1% concentration (a) and 0.3% of bare MNPs (b) respectively.....	45

Figure 3.20: Propagation of the shear wave in the phantom with 4% of gelatin and 1 % of nanoparticles (MNPs-100NRL) as an inclusion in 19 ms .....	46
Figure 3.21: Displacements of the shear wave in the phantom for 4% of gelatin and 1% concentration of MNPs -100NRL (a) and frequency of the magnetic nanoparticles movement (b).....	46
Figure 3.22: Propagation of the shear wave in the gelatin phantom (4%) and 1% of nanoparticle (MNPs-NRL800) as an inclusion in two different times.....	47
Figure 3.23: Displacement of the shear wave in the gelatin phantom (4%) and 1% concentration of MNPs 800NRL (a) and frequency of the magnetic nanoparticles movement (b).....	47
Figure 3.24: Shear wave velocities in a dispersive medium with 4% gelatin and 2% agar for phantoms including MNPs, MNPs-100NRL and MNPs-800NRL.....	48
Figure 3.25: The direct relation of magnetic on the induced displacements.....	49
Figure 3.26: The shear wave propagation through the phantom with 0.2% nanoparticle (MNPs-800NRL) as an inclusion in 19 ms.....	49
Figure 3.27: Displacements of the shear wave in the phantom with 1 % concentration using of MNPs -800NRL (a) and frequency of the magnetic nanoparticles movement (b).....	50
Figure 3.28: The displacement amplitude detected in phantoms with different concentration of MNPs-800NRL.....	50

---

# LIST OF TABLES

---

Table 2.1: Characteristics of the multi-layer coil.....	21
Table 2.2: The properties of superparamagnetic nanoparticles used in the phantoms.....	23
Table 2.3: Characteristics of the multi-layer coil of the magnetic excitation system.....	27
Table 2.4: Characteristics of the used transducers coupled to Sonix RP.....	27
Table 3.1: Mechanical properties of phantoms with 4% gelatin.....	48
Table 3.2: A resume of all used phantoms and physical parameters .....	5

## Table of contents

1. Intruduction.....	1
1.1. Ultrasound Imaging.....	1
1.1.1. Basics of Ultrasound Imaging.....	1
1.2. Physics of Ultrasound Elastography.....	2
1.3. Viscoelasticity.....	5
1.4. Elastographic techniques.....	8
1.4.1. Static elastography.....	8
1.4.2. Dynamic elastography.....	9
1.5. Phantoms.....	11
1.6. Magnetic nanoparticles.....	12
1.7. Magneto Motive Ultrasound Imaging.....	14
1.7.1. Application of MMUS.....	17
1.8. Objective.....	19
2. Materials and Methods.....	20
2.1. Experimental Setup.....	20
2.2. The magnetic field.....	22
2.3. Magnetic nanoparticles ( $Fe_3O_4$ ).....	22
2.4. Tissue mimicking phantom.....	23
2.4.1. Gelatin tissue mimicking phantom.....	24
2.5. Ultrasound system.....	27
2.5.1. High framerate.....	29
2.6. Particle displacement.....	29
2.7. Shear wave velocity and viscoelastic parameters.....	33
3. Results and Discussion.....	35
3.1. Analysis of magnetic field of excitation coil.....	35
3.2. Evaluation of acquisition system.....	36
3.3. Evaluating phantoms for SDMMUS imaging.....	36
4. Conclusion.....	52
5. References:.....	54

# ***1. Introduction***

## ***1.1. Ultrasound Imaging***

Imaging modalities including magnetic resonance imaging (MRI), X-ray computed tomography (CT) and ultrasound (US) are valuable techniques to detect pathologies such as cancers, tumors and etc. in early stages. Among all, ultrasound is more widely used because of having a better temporal resolution, lower costs and not using ionizing radiation [1, 2]. However, ultrasound is limited in contrast, some contrast agents have been introduced to address this issue. The more details about these contrast agents and how they address these limitations will be discussed in following sections.

### ***1.1.1. Basics of Ultrasound Imaging***

Ultrasonic waves are mechanical vibrations with a frequency greater than 20 kHz, frequencies above those audible by humans. The range of frequency used in medical diagnostic ultrasound imaging is 2-15 MHz. The clinical diagnostic ultrasound equipment consist of a computer, a monitor and a transducer (probe) contains multiple piezoelectric elements. When an oscillating voltage is applied to these elements, they vibrate and produce a sound waves that travel outward. Inversely, when sound waves hit the piezo element, a voltage is generate. Consequently, the same piezo element can be used to transmit and receive sound waves. In general, medical ultrasound machines use a wave frequency range from 1 – 12 MHz and consider the speed of sound for soft biological tissue of 1,540 *m/s* [3].

In this thesis, a radiological ultrasound system with programmable platform dedicate to research was used. To produce an ultrasound image, short pulses of ultrasound (US) waves through medium are transmitted by an ultrasound transducer. During the propagation, part of the ultrasonic energy returns to the transducer due to the spreading of the waves by the internal structures of the medium with different acoustic impedances. Then, the back scattered echoes are detected by the same probe applied for sending the ultrasound waves. Therefore, the amplitude of the reflected pulse is determined by the difference in acoustic impedance between two media to generate the B-mode image [4]. If two tissues have identical acoustic impedance no echo is produced. While, considering a medium with a large difference in acoustic impedance like soft tissue/air almost all reflection of the ultrasound pulse occur. Hence, in an ultrasound image the difference in the density and speed of sound at tissue boundaries is a fundamental property that generates echoes and contrast [5].

When an acoustic wave propagates through a soft tissue, the energy associated with the beam is reduced or attenuated as a function of distance. There are some mechanisms that cause this loss of energy including absorption which is the most important mechanism, scattering and reflection [5].

This reduction in amplitude of wave versus distance is exponential in nature (equ.1.1). The rate at which the pressure of the wave is attenuated, is specified as the attenuation coefficient and can be expressed in dB per cm or a unit of nepers per centimeter which is described below [6],

$$p(x) = p_0 e^{-\alpha x} \quad (1.1)$$

where  $p_0$  is the wave pressure at some reference point (e.g., at the transmitting surface of transducer) and  $p(x)$  is the wave pressure at distance  $x$  from that. The attenuation coefficient has a unit of nepers per centimeter and is sometimes expressed in relative scale of decibels per centimeter or

$$\alpha\left(\frac{dB}{cm}\right) = 20(\log_{10} e)\alpha\left(\frac{np}{cm}\right) = 8.686\alpha\left(\frac{np}{cm}\right) \quad (1.2)$$

Some studies have shown that scattering contributes little to attenuation in most soft tissues [7]. Therefore, it is safe to say that absorption is the dominant mechanism for ultrasonic attenuation in biological tissues [7].

Also, the relation between the attenuation coefficient and frequency can be described by the following equation:

$$\alpha(f) = af^b \quad (1.3)$$

As can be seen, the attenuation coefficient is dependent on the frequency of the mechanical wave ( $f$ ), where  $a$  and  $b$  are empirical constants whose values differ from one type of tissue to another [8].

It should be mentioned that, to have a better resolution (the ability to show closely spaced targets separately in the image), a high frequency (short wavelengths) ultrasound beam can be considered. However, the depth of wave penetration is significantly reduced at higher frequency.

## ***1.2. Physics of Ultrasound Elastography***

Elastography estimates the elasticity of the tissue which describes tendency of tissue to resume its original size and shape after removal of the force. The change in size or shape is known as the strain [8], which is expressed as a ratio in equation 1.4 [9]:

$$\varepsilon = \frac{\Delta L}{L} \quad (1.4)$$

Considering Hooke's law [10], assuming that a material is totally elastic and its deformation has no time dependency (i.e., viscosity) the elasticity can be expressed [9]:

$$\sigma = E \cdot \varepsilon \quad (1.5)$$

where stress ( $\sigma$ ) is the force per unit area with units' Pascals (i.e. N/m<sup>2</sup>), strain ( $\varepsilon$ ) is the expansion per unit length which is dimensionless, and the elastic modulus ( $E$ ) correlates stress to strain with units' kilopascals.

The modulus of the elasticity is classified in three types, regarding to the nature of force applied on the medium as follows: 1. Young's Modulus (longitudinal elasticity)  $E = \text{stress}/\text{strain}$ , 2. Shear modulus (rigidity,  $G$  or  $\mu$ ) and, 3. Bulk or volume modulus ( $K$ ) describes the change in volume of a material to external stress [11]. For an isotropic homogenous material, the relationship between these moduli are defined in the equation (1.6) and (1.7) [7], [8]:

$$G = E / (2(1 + \sigma)) \quad (1.6)$$

$$K = E / (3(1 - 2\sigma)) \quad (1.7)$$

where  $\sigma$  is near 0.5 for incompressible medium. Then,  $E = 3G$ , and the ratio of  $E/K$  is approximately 0 for a soft tissue (eq. 1.7). The higher the elastic modulus  $E$ , the more a material tends to resist deformation, which can be thought of as increased stiffness.

Bulk modulus is typically several orders of magnitude larger than shear modulus in tissues, therefore, the velocity of longitudinal wave is almost totally determined by the bulk modulus of the tissues [13]. According to how particles in the solid move during wave propagation, solids can support mechanical waves in two main principals' modes. When, the particles of the medium oscillate along the direction of propagation of the wave, a longitudinal pressure wave (a) is created [8]. Figure 1.1 depicts a shear wave (b) , in which the oscillatory motion of the

particles in the medium is perpendicular to the wave propagation [8]. Conventional ultrasound produces both longitudinal and transverse waves. However, the generated shear waves by conventional ultrasound are highly attenuated in soft tissues at diagnostic imaging frequencies, since shear wave attenuation coefficients increase with frequency [14].

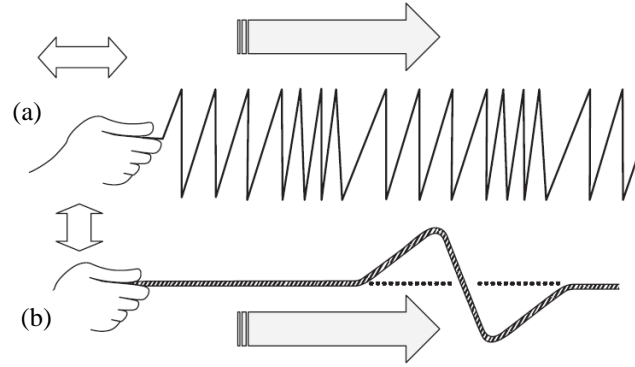


Figure 1.1: Longitudinal wave (a) and shear wave (b) Adopted from [8] .

For longitudinal waves (compressional waves), the speed  $C_l$  depends on the density of the medium ( $\rho$ ) and compressibility ( $\kappa$ ), Eq. 1.8. While for shear waves, based on the Eq.1.9, the speed of propagation depends on shear modulus  $\mu$  and density  $\rho$  [8].

$$C_l = \sqrt{\left(\frac{\kappa}{\rho}\right)} \quad (1.8)$$

$$C_s = \sqrt{\frac{\mu}{\rho}} \quad (1.9)$$

Longitudinal waves are also called primary waves/P waves and the shear waves are known as secondary waves/S waves [6, 15]. Typically in biomaterials and materials including soft tissue mimicking characteristics such as phantoms, the velocity of the longitudinal wave is much higher than the velocity of the shear waves. In some soft tissues the velocity for the compressional wave is in the order of 1470 m/s to 1580 m/s while this range is 1 m/s to 20 m/s for the transverse velocity [5]. However, Eq.1.9 is accurate only when viscosity and the medium is isotropic and linear regime, another mechanical properties of tissue, is ignored [16, 17].

### ***1.3. Viscoelasticity***

Estimation of viscoelastic properties of materials plays an essential role in material science and medical diagnosis. Specifically, a target's shear elasticity (i.e. stiffness) and shear viscosity (i.e. viscosity) can be estimated from the resultant displacement from an applied force. Since the viscoelasticity of soft tissues is often associated with pathological state, they can be used as a diagnostic tool in medicine [18] .

Viscoelastic materials show three unique mechanical behaviors. (a) When a material is suddenly strained and then the deformation is maintained constant thereafter, the corresponding stresses induced on the material decrease with time, this phenomena is called stress relaxation; (b) when the material is suddenly stressed and then the stress is held constant afterward, the material continues to deform, and this phenomenon is known as creep; (c) the third phenomenon is called hysteresis and occur when the material is subjected to a cyclic loading, the stress-strain relationship in the loading and unloading process will be different and mechanical energy losses happen in the form of heat, Figure 1-2 (right). The area confined between ascending and descending curves is the energy observed by the matter and most of it is converted into heat. The characteristics of hysteresis, creep and relaxation, can be observed in many materials. Concertedly, they are called features of viscoelasticity [8, 19].

Since biological tissues contain a mixture of solid and fluid material, they should be described in terms of both elasticity and viscosity [16]. A model of linear viscoelasticity can be made by considering combinations of the linear elastic spring and the linear viscous dash-pot [19].

Viscoelastic materials show time-dependent material behavior; i.e. after applying force on a viscoelastic material, the response of this material depend on the stress magnitude and how fast the stress is applied to or removed from the material. Hence, for a viscoelastic material, the stress–strain relationship is not unique but is a function of the time. While an elastic material has a unique stress–strain relationship and it is not dependent on time. Also, for an elastic material, as can be seen in Figure 1.2 (left) loading and unloading paths coincide. Hence, throughout loading and unloading no loss of energy is illustrated [6, 17].

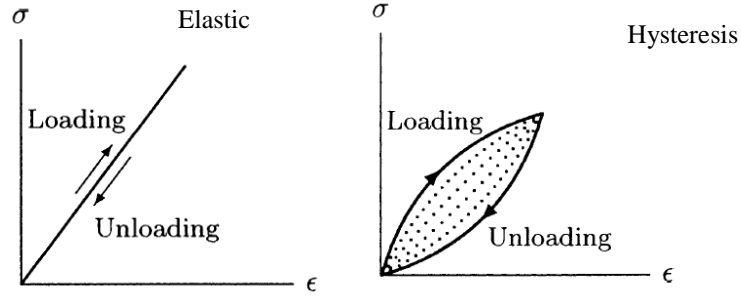
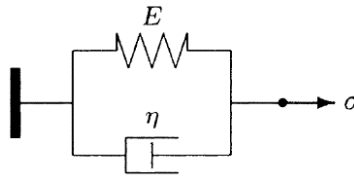


Figure 1.2: Strain – stress relationship for an ideal elastic material (left). Illustrating hysteresis, strain –stress relationship for a viscoelastic material (right) Adopted from [19].

There are three mechanical models that are often used to describe the viscoelastic behavior of materials including Kelvin-Voigt Model, Maxwell Model and standard Solid Model [19]. To the best of our knowledge and based on literature review [20–23], the Kelvin Voigt showed more satisfactory results for viscoelastic materials than the others and it will be use in this thesis for evaluating the viscoelastic parameters. Therefore, we will only discuss the Voigt Model. This model consisted of a spring and a dashpot connected in parallel arrangement, Figure 1.3. The strain-strain relationship for the Kelvin-Voigt models can be defined as [22]:

$$\sigma = \left( \mu_1 - \mu_2 \frac{\partial}{\partial t} \right) \varepsilon \quad (1.10)$$

Where stress  $\sigma$  is associated to the strain  $\varepsilon$ ,  $\mu_1$  is shear elasticity,  $\mu_2$  is shear viscosity and time-derivative operator  $\partial / \partial t$ .



Kelvin-Voigt model

Figure 1.3: A schematic of Kelvin-Voigt model

Using the one-dimensional Helmholtz equation [22]. The map of elasticity is achieved in dynamic elastography [22]:

$$\frac{\partial^2 FT_t(u_z(x))}{\partial x^2} + k^2 FT_t(u_z(x)) = 0 \quad (1.11)$$

Where  $FT_t$  is time Fourier transform,  $u_z$  is the transverse displacement, and the longitudinal coordinate is defined by  $x$ .  $k$  is the wave number and is real and constant, but it can be complex in the case of soft tissues when the propagation medium is an energy absorber. Then,  $k$  is described as complex wave vector [24]:

$$k = \sqrt{\frac{\partial^2 FT_t(u_z(x))}{\partial x^2} / FT_t(u_z(x))} \quad (1.12)$$

In the case of linear viscoelastic medium the wave number  $k$  is complex, written as [25]:

$$k^* = k_r - ik_i \quad (1.13)$$

where  $k_r = \omega/c_s$ ,  $k_i = \alpha$ , Shear modulus can alternatively be defined as:

$$\mu = \rho \frac{\omega^2}{k^2} \quad (1.14)$$

Because  $k$  is a complex quantity, the shear modulus also becomes a complex quantity and complex shear modulus,  $\mu^*(\omega) = \mu_1 + i\omega\mu_2$ , are related [26–28]. Where  $\mu_1$  is defined as shear elastic or storage modulus and  $\mu_2$  as shear viscous or loss modulus [11, 29]:

$$\mu_1 = \rho\omega^2 \frac{k_r^2 - k_i^2}{k_r^2 + k_i^2} \quad (1.15)$$

$$\mu_2 = \rho\omega^2 \frac{k_r^2 - k_i^2}{(k_r^2 + k_i^2)^2} \quad (1.16)$$

The velocity of the transverse wave and attenuation for the Kelvin-Voigt model is described [24]:

$$c_t^{Kelvin-Voigt} = \sqrt{\frac{2(\mu_1^2 + \omega^2\mu_2^2)}{\rho(\mu_1 + \sqrt{(\mu_1^2 + \omega^2\mu_2^2)})}} \quad (1.17)$$

$$\alpha_s(\omega) = \sqrt{\frac{\rho\omega^2 \sqrt{\mu_1^2 + \mu_2^2}}{2(\mu_1^2 + \mu_2^2)} - \mu_1} \quad (1.18)$$

$\rho$  is the density of the medium and  $\omega$  is angular frequency of vibration.

Therefore, regarding to Eq. 1.17 it is noticeable that in tissue viscoelasticity, the speed of shear wave depend on the frequency because of dispersive nature of biological tissue [30, 31]. Hence, a broad range of frequencies is needed for evaluating the shear elasticity and viscosity. While as discussed earlier in equation 1.9, the velocity of shear wave is proportional to the square root of the elastic constant and is independent of the vibration frequency.

#### ***1.4. Elastographic techniques***

Elastography by ultrasound is a procedure to measure the response of a tissue to an excitation force which was developed by Ophir et al. [32]. The way in which the tissue deforms provide information about the mechanical properties of tissue. It is based on the Palpation, the oldest clinical method which has been used to evaluate changes in the tissue stiffness. However, this procedure is being limited for lesions which are located in deep regions and having too small size [33]. After Ophir's work, several elastography techniques have been established and classified based on the mechanical excitation type (static, dynamic, transient vibration or acoustic radiation force) and how these excitations are produced (externally or internally) [14, 34, 35]. In all methods, the resulting tissue motions can be tracked using optical [36], ultrasonic [35] and magnetic resonance imaging (MRI) [35]. US elastography methods are the most common methods [33].

A brief discussion about elasticity techniques are discussed below:

##### ***1.4.1. Quasi-Static elastography***

In Quasi-static ultrasonic elastography, an external compression is induced to tissue. In this technique, by comparing images taken before and after mechanical load to the tissue, the strain is determined. Using this tissue strain, an elastographic image can then be generated which is also referred as an elastogram. On an elastogram, low strain (hard tissue) values are displayed as dark on the image and large strain (soft tissue) values are bright. It is a qualitative technique to obtain information about the stiffness contrast between normal and abnormal tissues and also suitable to superficial organs [32]. This modality is very operator dependent i.e., based on

the experience and researchers' techniques the quality of result will be achieved. It means proper compression strength and right angle of compression is needed to avoid misinterpretation [38 , 36].

#### ***1.4.2. Dynamic elastography***

Dynamic methods have potential to explore the dynamic properties of the medium such as viscosity. Techniques of dynamic excitation induce harmonic vibrations, often in the range of 50 to 500 Hz, and create an image of the shear wave's propagation due to the excitation throughout the whole system [35]. These techniques include magnetic resonance elastography (MRE) [34] , vibration sonoelastography [39], Supersonic shear imaging (SSI)[40], Acoustic radiation force elastography (ARFI) [41], Sonoelasticity [39], shear wave elasticity imaging (SWEI) [42] and Shear wave dispersion ultrasound vibrometry (SDUV) [30].

##### ***1.4.2.1. Acoustic radiation force elastography***

A method that uses focused ultrasound to produce an acoustic radiation force to push the tissue, and measures the resulting deformation to evaluate the mechanical properties of the tissues. An advantage of this method is that the tissue displacement is created at the location of interest. In this way, the generated vibrations will be independent of the shear wave attenuation between excitation point and region of interest [14]. Several techniques based on radiation force have been developed including, SWEI, vibroacoustography, supersonic shear imaging (SSI), sonoelasticity and SDVU.

Elastography and ARFI do not acquire a quantitative measure of tissue stiffness; typically obtain a relative map of tissue stiffness [17].

##### ***a. Sonoelastography***

In sonoelastography a mechanical source applied to induce a low-frequency vibration. In this technique, a Doppler ultrasound is used to evaluate the motion amplitude and phase within the region of interest. This method has limitations such as the non-uniform vibration produced by the source and is attenuated by tissues [42, 43].

##### ***b. Supersonic shear imaging***

Supersonic shear imaging (SSI) relies on the acoustic radiation force to remotely generate low-frequency shear waves in tissue that is imaged at a high frame rate (5000 frames per second) and can be acquired using the same piezoelectric arrays as the ones used in conventional ultrasonic scanners. This radiation force acts as a dipolar source of shear waves and mainly radiates in transverse directions [46].

Sonoelastography and SSI can provide maps of shear modulus and viscosity, but specialized hardware is necessary to implement both methods [47].

***c. Vibroacoustography Imaging***

Fatemi and Greenleaf [33] developed vibroacoustography technique which is a highly sensitive low-frequency ARFI method. In this technique, acoustic emission is produced by focusing two different ultrasound beams of slightly different center frequencies at the same point and vibrating the tissue which can be detected with an external hydrophone [8].

***d. Shear wave elasticity imaging***

Sarvazyan et al [42] have established this technique, that structures of tissue characterized and imaged through shear waves induced remotely by the radiation force of a focused ultrasonic beam. It should be mentioned that the difference between SWEI with ARFI is that, SWEI is based on the use of shear wave propagation laterally from the beam axes and measuring shear wave propagation parameters to create elasticity map, while in ARFI elasticity information obtains from the axis of pushing beam and applies multi pushes to generate a 2-D stiffness map.

***e. Shear wave dispersion ultrasound vibrometry***

Chen et al, have established shear wave dispersion ultrasound vibrometry (SDUV) which uses ultrasound radiation force to produce a harmonic shear wave and measure its propagation [29, 30]. This is performed at multiple frequencies to analyze the dispersion of the shear wave velocity, and then those values are fit by a model to obtain the shear elasticity and shear viscosity of the tissue. A limitation of this method was that the modulation frequency had to be changed multiple times to evaluate the dispersion over a significant bandwidth. This method was advanced to make faster measurements by transmitting repeated tone bursts of ultrasound [30].

***1.4.2.2. Magnetic resonance elasticity***

A conventional MRI system is used with an additional Motion Encoding Gradient (MEG), and a vibration device is used to mechanically excite the tissue. A vibration actuator creates shear or compression waves in the object at the same frequency as the MEG. Synchronization is achieved by triggering the actuation device from the image sequence [47, 48] . Any cyclic motion in the presence of the MEG generates a phase shift in the signal from which it is possible to calculate the displacement at each voxel and directly image the shear waves within the tissue

of interest. The phase MEG measures the mechanical vibration and the magnetic resonance image data is post-processed so that the phase and the amplitude of vibration can be acquired. Finally, an inversion algorithm based on measured displacements is applied to calculate the shear modulus distribution of the tissue [50].

Sensitivity is the main advantage of this technique, it can detect motion in the order of hundreds of nanometers. However, the long acquisition time (20 minutes) limits the application to static organs. Moreover, there is a further weakness of this technique because when waves are reflected from internal tissue boundaries, they can interfere constructively and destructively and influence the shear modulus calculation [51].

#### ***1.4.2.3. Transient Elastography (TE)***

Transient Elastography [52] is a quantitative method [52–55] that used a low frequency mechanical vibration system with pulsed excitation and ultrasound to track the shear wave displacement by the medium under analysis, determining the wave velocity and the elasticity of the medium.

### ***1.5. Phantoms***

Since 1960, tissue phantoms have been developed to characterize and calibrate the ultrasound imaging. Phantoms are also used to help in the development of new ultrasound transducers, systems or diagnostic techniques [57].

Soft tissue phantoms are used to analyse the viscoelastic behavior of biological tissues [57,58]. In the ultrasonic elastography, phantoms are widely used that mimic either the normal tissue or lesions. Hydrogels, are very common to design phantoms because of being very similar to tissues in many aspects such as acoustic and elastic properties [59].

There are two kinds of hydrogels: physical gels, which are obtained through physical procedures such as heating and cooling (e.g. gelatin, agar), and chemical gels, which are attained through chemical reactions including polymerization (e.g. Polyacrylamide) [60]. Since probably the preparation processes of physical gels are much simpler and safer than chemical ones the physical gels are usually more preferred for tissue-mimicking phantoms. However, chemical gels are much more stable than physical gels and are easier to preserve once prepared. Therefore, they are also an alternative solution for tissue-mimicking phantoms in ultrasonic elastography [61].

Therefore, many works have been done on the construction of phantom, because of having characteristics such as speed of sound and attenuation similar to those obtained in human soft

tissues [59]. Moreover, since tissue-mimicking phantoms are easily accessible and convenient to handle, they are appropriate for elastography modalities [62].

### 1.6. Magnetic nanoparticles

Magnetic materials are categorized into five different types in terms of their magnetic properties namely diamagnetism, paramagnetism, ferromagnetism, anti-ferromagnetism and ferrimagnetism [42, 43] which are classified by their susceptibility to magnetic fields.

Diamagnetic materials show a weak repulsion in an external magnetic field (negative susceptibility), for example water, NaCl, H<sub>2</sub> and N<sub>2</sub> [65].

Paramagnetic materials exhibit a small and positive susceptibility in an external magnetic field and attracted weakly by the field, examples of paramagnetic materials are manganese, aluminum and alkaline earth metals [65].

In ferromagnetic materials their susceptibility is much larger than other magnetic materials, therefore show a strong attraction to an external magnetic fields. Iron (Fe) is one of the most important ferromagnetic substances, however, there are other ferromagnetic elements including Ni, Co and their alloy with Fe [65].

Ferrimagnetic materials usually have a similar magnetic behavior to ferromagnetic materials except for a smaller magnetization value. While, Anti-ferromagnetism shows a small and positive susceptibility in the external magnetic field [65].

In ferri-ferromagnetic material when a sufficiently large magnetic field is applied, the spins within the materials align with the field. By removing the external magnetic field, their overall magnetization value is randomized to zero [65, 66]. In Figure 1.4 the magnetic behavior of materials in exposure of an external magnetic field can be observed.

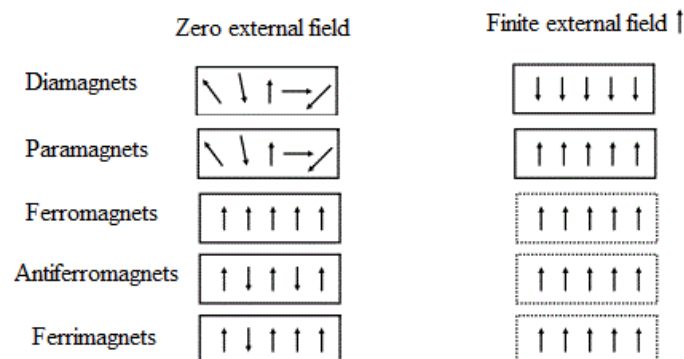


Figure 1.4: The behavior of magnetic material in exposure of an external magnetic field.

One of the most important properties of ferromagnetic and ferrimagnetic materials is that the internal magnetic moments can be induced by a small external magnetic field. Such remarkable property is due to the existence of small magnetic regions called magnetic domain. Ferromagnetic and ferrimagnetic materials exhibit multidomain, single domain, and superparamagnetic properties, as the size of the specimen is reduced to below a critical size [65].

Nanoparticles (NPs) are usually defined as particles with sizes between 1-100 nm in which the material shows novel properties which are very different from their bulk counterpart. Magnetic properties of the nanoparticles can also be more complicated than those of their bulk. In fact, all relevant magnetic properties (coercivity, blocking temperature, saturation and remanent magnetizations) are functions of particles' size and shape and of surface chemistry [67, 68]. For example as size reduces to a definite size, nanoparticles exhibit the so-called superparamagnetic regime, which is of great interest in biomedical application [70].

Although there is a strong and relatively well-established dependence of magnetic properties on the size of the nanoparticles, magnetic behavior is complicated and cannot be defined with respect to one parameter. There are other factors that play an important role on the magnetization of particles such as morphology, composition, degree of crystallinity, core-shell design and surface coating of magnetic nanoparticles [71].

Superparamagnetic nanoparticles have demonstrated great promise in biology and medicine applications including protein purification, bacterial detection, drug delivery, hyperthermia [72]. In addition, there are various imaging techniques such as positron emission tomography (PET), magnetic particle imaging (MPI), single photon emission computed tomography (SPECT) optical imaging, magnetic resonance imaging (MRI) [70] and magneto motive ultrasound (MMUS) [73]. MMUS is one of the recent modality which benefits from superparamagnetic nanoparticle as contrast agent to visualize molecular and cellular levels through ultrasound imaging.

Among various functional magnetic nanoparticles (MNPs), superparamagnetic magnetite ( $\text{Fe}_3\text{O}_4$ ) nanoparticles (with sizes less than 49 nm) have attracted more attention because they can be designed as a highly biocompatible material with high magnetization, and low toxicity to be used in specific application [67, 68, 73, 74]. Meanwhile, superparamagnetic nanoparticles are of great interest in biomedical application because after eliminating the magnetic field, particles will not show any magnetic interaction after removing the external magnetic field.

The stabilization of superparamagnetic NPs by surface coating is a crucial issue because these particles tend to aggregate when dispersed into high ionic strength solvents. Many researchers

have attempted to prepare superparamagnetic nanoparticles with high stability and biocompatibility [69]. Several coating materials have been used to modify the surface chemistry of the MNPs such as organic surfactants (sodium oleate), inorganic metals (gold), inorganic oxides (silica), bioactive molecules (liposomes), polymeric coating (polyethylene glycol, polyvinyl pyrrolidone and dextran) and some plants extracts that obtained from *Syzygium cumini*, *Eleaocarpus sphaericus* and *Hevea brasiliensis* [75, 76].

Natural rubber latex (NRL), extracted from a native tree (*Hevea brasiliensis*), is a naturally occurring form of the cis-1,4 polyisoprene and consists of rubber molecules (cis-isoprene), water and non-rubber constituents such as protein, lipids, and carbohydrates [78]. NRL has some biomedical and industrial applications such as drug delivery systems in guided bone regeneration (GBR) [79], biomaterial in vascular prosthesis fabrication [80], manufacturing of tires, balloons, aircrafts and surgical gloves [81]. In this thesis, we used superparamagnetic ( $\text{Fe}_3\text{O}_4$ ) nanoparticles covered by NRL as contrast agents for SDMMUS.

### ***1.7. Magnetomotive Ultrasound Imaging***

As discussed earlier in section 1.1, although ultrasound imaging has several advantages including real time, cost effectiveness, portable, reasonable penetration depth and excellent temporal resolution, it has a drawback of being limited in contrast. Meanwhile, some contrast agents have been developed to detect the cellular and molecular levels such as microbubbles, liposomes, perfluorocarbon droplets and magnetic nanoparticles, however, these contrast agents have also some obstacles which will be explained briefly.

Microbubbles as the most widely used US imaging contrast agents [82] can generate significant contrast because of having a large acoustic impedance mismatch between the microbubbles and their surroundings. However, they are limited because of their large size, larger than 1  $\mu\text{m}$  [83] and also short lifespans in the body [73]. Although liposomes have developed a longer lifespan than microbubbles, they are still too large to pass through endothelial gap junctions in the leaky vasculature of pathologies [72].

Nano-sized perfluorocarbon droplets (PFC) and silica nanoparticles have been introduced to overcome the effects of size and improving the enhancement imaging efficacy but in this case a significant contrast cannot be obtained in ultrasound images due to the weak ultrasound reflections [84].

Finally, using superparamagnetic nanoparticles as contrast agent in conventional ultrasound is not possible because particles are too small to backscatter ultrasound at a detectable level

[72, 81]. Although in MRI superparamagnetic agents within label molecules and cells are used to detect changes in magnetic properties of tissue [84, 85], MRI-based molecular imaging modalities cannot obtain cellular and molecular information in real time and also they are expensive [87]. Therefore, magneto motive ultrasound imaging (MMUS) [73] was proposed as an imaging technique to overcome this issue. In this technique, in order to induce a motion within the tissue labeled with magnetic nanoparticles a magnetic excitation is applied and the backscattered ultrasound radio frequency (RF) waves are used to localize and image the magnetically induced motions within the tissue. These vibrations, in the order of micro meters, are originated from the interaction of the particles with an external oscillating magnetic field. A burst of magnetic field pulses or a continuous-time harmonic magnetic field with frequencies in order of few Hertz usually excites the magnetic nanoparticles [88]. Therefore, this method is an indirect way to detect the nanoparticles within in the tissue because the induced vibration in the medium surrounding the nanoparticles is detected rather than particles. The magnetically induced motion detected in the MMUS image depends on the magnetic susceptibility and concentration of the magnetic nanoparticles within the tissue. Due to their weak diamagnetic properties, normal tissue constituents do not respond to the magnetic field. However, when tissue is labeled with magnetic nanoparticles, it tends to move towards the lower magnetic potential [87, 88].

As mentioned above, a time-varying magnetic field is used to induce a motion to the magnetic nanoparticles in MMUS. Thereafter, the particles start to vibrate and this movement can be detected with ultrasound. The motion of a magnetic particle depends on the spatiotemporal characteristics of the magneto-motive force and on the viscoelastic properties of the surrounding tissue. The magneto-motive force ( $F_m$ ) acting on a magnetic nanoparticle and resulting in displacement of tissue can be defined as:

$$F_m = (m \cdot \nabla) B \quad (1.19)$$

where  $m$  is the magnetic moment and  $B$  is magnetic flux density.

Considering the  $z$ -directional component of the magnetic field ( $B_z$ ) and the magnetic moment ( $m_z$ ), the magneto-motive force  $F_{mz}$  acting in  $z$ -direction can then be expressed as  $F_{mz} = (m_z) B_z$ . For a magnetic nanoparticle located in a weakly diamagnetic medium such as tissue, the magnetic moment,  $m_z$  can be written as  $m_z = V_m M_z$  where  $V_m$  is the volume of the magnetic portion of the nanoparticle and  $M_z$  is the  $z$ -directional volumetric magnetization.  $V_m$  can be described as  $V_m = V_{np} \times f_m$  where  $V_{np}$  is the total size of the nanoparticle and  $f_m$  is a

dimensionless factor, expressing the volumetric ratio of magnetic material in a nanoparticle. The z-directional volumetric magnetization,  $M_z$ , can be described as  $M_z = (\chi_{np} - \chi_{medium}) H_z$ , where  $H_z$  is the strength of the magnetic field in z direction and  $\chi_{np}$ ,  $\chi_{medium}$  are susceptibility of the volume magnetic of the nanoparticle and medium respectively. Since the medium is considered weakly diamagnetic,  $|\chi_{np}| \gg |\chi_{medium}|$  and consequently  $\chi = \chi_{np}$  where  $\chi_{np}$  is the volume magnetic susceptibility of the nanoparticle. Assuming that  $B_z$  does not change significantly over the nanoparticles due to its small size, the volumetric magnetization  $M_z$  can be written as  $M_z = \lambda_{np} \frac{B_z}{\mu_0}$  where  $\mu_0$  is the permeability of free space ( $4\pi \cdot 10^{-7} \text{ N/A}^2$ ). Hence, the magnetic force acting on the nanoparticle due to the magnetic field can be defined as:

$$F_{mz} = \frac{V_{np} f_m \chi_{np}}{\mu_0} (B_z \cdot \nabla) B_z \quad (1.20)$$

Since

$$(B_z \cdot \nabla) B_z = \frac{1}{2} \nabla (B_z \cdot B_z) = B_z \frac{\partial B_z}{\partial z} \quad (1.21)$$

Equation (1.20) can be simplified to:

$$F_{mz} = \frac{V_{np} f_m \chi_{np}}{\mu_0} B_z \frac{\partial B_z}{\partial z} \quad (1.22)$$

If we suppose a sinusoidal magnetic field with frequency  $\omega$  along the z direction as excitation field has been applied as given:

$$B(z, t) = \sin(\omega t) B_z(z) \quad (1.23)$$

the magnetic force ( $F_{mz}$ ) can be expressed as:

$$F_{mz} = \frac{\chi_{np} f_m}{2\mu_0} (1 - \cos(2\omega t)) B_z(z) \frac{\partial B_z(z)}{\partial z} = \frac{\chi_{np} f_m}{2\mu_0} (1 - \cos(2\omega t)) B_z(z) \frac{\partial B_z(z)}{\partial z} \quad (1.24)$$

Based on Eq. (1.24), which define the magnetic force acting on a nanoparticle, it follows that the total force ( $F_{tot}$ ) acting on the particle in a surrounding material can be described as [72, 89]:

$$F_{tot} = \frac{\chi_{np} V_{np} f_{np}}{2\mu_0} (1 - \cos(4\pi f t)) B_z(z) \frac{\partial B_z(z)}{\partial z} - k_z(t) - s \frac{\partial z}{\partial t} \quad (1.25)$$

where  $k_z(t)$  is an elastic restoring force of the medium and  $s \frac{\partial z}{\partial t}$  is a viscous drag force [73].

Eq. (1.25) illustrates some important aspects for MMUS modality. Firstly, magnetic force acting on the magnetic nanoparticle is linearly proportional not only to the magnetic susceptibility of the nanoparticles ( $\chi_{np}$ ), but also to their geometry and structure ( $V_{np}$  and  $f_m$ ). Clearly, nanoparticles with larger magnetic core size and higher susceptibility will produce larger magnetic force and therefore, larger displacement and resulting in a high contrast. However, increasing the size of the nanoparticles has some limitations for specific labeling [1]. Therefore, the magnetic susceptibility of nanoparticles plays a more important role in determining the sensitivity of the MMUS imaging technique. However, safety and toxicity issues of these materials are still subject to more investigations.

Second, magnetic force acting on nanoparticle is proportional to both the magnitude ( $B_z$ ) and the gradient ( $\partial B_z / \partial z$ ) of magnetic flux density, namely the larger is the field and the gradient of the field, the larger is the magnetically induced motion. Finally, the frequency response of the force acting on the superparamagnetic nanoparticles is exactly twice the externally applied modulation frequency. This relationship can be used as a reliability of the observed magneto-motive response of magnetic nanoparticles in the medium due to the magnetic field [92].

### ***1.7.1. Application of MMUS***

During last decade, several works have been performed on MMUS. Mehrmohammadi et al [92] used the MMUS modality to localize the motion of superparamagnetic nanoparticles with different concentration of  $Fe_3O_4$  labeled in tissue mimicking PVA phantoms. The same group, as a modified MMUS modality, applied a pulsed magnetic field instead of an a harmonic magnetic field for MMUS system to detect the motion of magnetic nanoparticles embedded in the viscoelastic medium [93]. Also, they demonstrated clusters of superparamagnetic nanoparticle resulted in higher displacements for MMUS compared to those which didn't form clusters with the same amount [90]. The first *in vivo* measurement of this group [94] was reported by Pulsed MMUS using superparamagnetic zinc substituted magnetite nanoparticles with enhanced magnetic saturation as a contrast agent and improved the signal to noise ratio (SNR). Lately, zinc substituted magnetite nanoparticles prepared with coprecipitation method

were used for MMUS imaging in tissue-mimicking oil-based gel phantoms and the crucial role of magnetization was demonstrated [95]. Moreover, the MMUS technique has also been combined with photoacoustic imaging [96]. To enhance the localization precision of the magnetic source in the body during gastro intestinal transit evaluation, a method was developed to acquire simultaneously the images of MMUS with the AC biosusseptometry [97]. Detecting the sentinel lymph nodes (SLN) through MMUS and MRI in rats and also testing how different injected concentrations of NPs affect the MMUs and MRI images were investigated by Evertsson [98].

In 2014, Almeida et al [99]. In our group proposed a technique called shear wave dispersion magneto motive ultrasound (SDMMUS) which is a subdivision of MMUS. This technique is used to estimate the mechanical properties of the medium. In this remote elastography novel method, interaction of the magnetic nanoparticles with an external magnetic field can generate a shear wave and propagation of this wave provides information about viscoelasticity properties of the medium including shear elasticity ( $\mu_1$ ) and shear viscosity ( $\mu_2$ ). Although several shear wave elastography methods have been established to estimate the mechanical properties of tissue using the speed of shear wave propagation which were discussed in chapter 1.4, in most of them the viscous behavior of the tissue, because of having limitations, has been neglected [100]. However, some techniques including MRE and SDUV [30] could overcome this issue by showing the importance of loss modulus in characterization of tissue. Compared to aforementioned techniques, SDMMUS has less complexity and is more cost effective with an acceptable accuracy. But to the best of our knowledge the only study using SDMMUS to estimate the mechanical properties of the medium is the earlier work in our group [21]. In that study, the feasibility of the method was proven using a gelatin phantom with 4 wt. % of the nanoparticles which were homogeneously dispersed in the whole phantom. Considering *in vivo* application, the nanoparticles were used are a huge concentration and not viable.

Therefore, in this thesis we investigated different sizes and shapes of phantoms as well as the kind and concentration of magnetic nanoparticles in order to optimize the generated shear wave and evaluate viscoelastic parameters. Because when generating a shear wave in a phantom, not only the shape and size of the phantom play a key role, but also the amount and magnetic properties of the nanoparticles should be taken into account. It is well known that there has been always a great attempt to decrease the dosage of NPs in biomedical application. Therefore, instead of using a homogenous phantom which contains a huge mass of nanoparticles to generate shear wave, we demonstrated that using only a small inclusion can

also produce a very good shear wave that can be used to estimate the mechanical properties of the medium.

### ***1.8. Objective***

In this thesis, we aimed to investigate various magnetic nanoparticles with different magnetic saturation as contrast agent in ultrasound imaging as well as to study the viscoelasticity properties of tissue mimicking phantoms. Here, we decreased the dosage of MNPs using an inclusion embedded in the phantom instead of using homogenously dispersed magnetic nanoparticles in the whole phantom. Furthermore, we examined the effect of magnetization on the induced displacement. In the end, we suggested one of the magnetic nanoparticles as an optimized agent to be used in both imaging and viscoelasticity property studies. Also, the limitation of our system was characterized by estimating the lowest possible concentration of the magnetic nanoparticle which can generate the shear wave.

## ***2. Materials and Methods***

### ***2.1. Experimental Setup***

A 3-D XYZ positioning system with 1.0 mm precision, was used to hold the tissue-mimicking phantom for experiments. As can be seen in Figure 2.1 (a-c), the magnetic field was generated by a multi-layer coil model S189.1 (manufacturer Solen Inc., Montreal, Canada) (Table 2.1). To be more precise, the coil has inner and outer diameters of 45 mm and 89 mm respectively, and height of 22 mm, with 9.1 mH of inductance,  $2.7 \Omega$  of impedance. A ferrite core of 1 cm diameter (manufacturer Thornton Eletrônica Ltda, São Paulo, SP, Brazil) with coercivity of 18 A/m is inserted in the center of the coil (Figure 2.1 (c)), which has been aligned with the field-of-view of the ultrasound transducer (L14-5/38). It should be noted that the ferromagnetic properties of a core with a high magnetic permeability led to the internal magnetic domains align with the external magnetic field as well as enhancing the local magnetic field. In this study, the tip of the ferrite core was positioned 3 mm away from the central region of the phantom. Then, the magnetic field gradient along the axial axis increase (chapter 1.7). As a result, with the increase of the gradient and the magnetic field in a small region, an increase in the intensity of the magnetic force was generated. The coil was driven by a function generator (Agilent, model 33522A, Santa Clara, Calif, Manufacturer), connected to a power amplifier (Ciclotron, model Dynamic 20000  $\Omega$ 2, class H, Barra Bonita, SP, Brazil). The trigger output of the generator was connected to the input trigger of the ultrasound system to synchronize the RF acquisition with the magnetic pulse. Using 10 cycles of sinusoidal voltage with different range of frequencies from 50 to 250 Hz, with a step of 50 Hz, to produce the magnetic excitation. The amplitude of the sinusoidal signal depends on the calibration curve and the frequency of the signal that will pass through the amplifier. During magnetic excitation, because of the current passing through the coil there is a mechanical vibration and this vibration may influence the measurement. Therefore, the coil has been isolated from the phantom being fixed separately to a platform that prevents transmission of mechanical noise.

Table 2.1: Characteristics of the multi-layer coil.

Model	S189.1
Number of turns	413
Wire AWG	18
Maximum current	10A
Inductance	9.1mH
Resistive impedance	2.7 $\Omega$
Dimensions	22 x 45 x 89 mm
Inner diameter	45 mm
Outer diameter	89 mm
High	22 mm

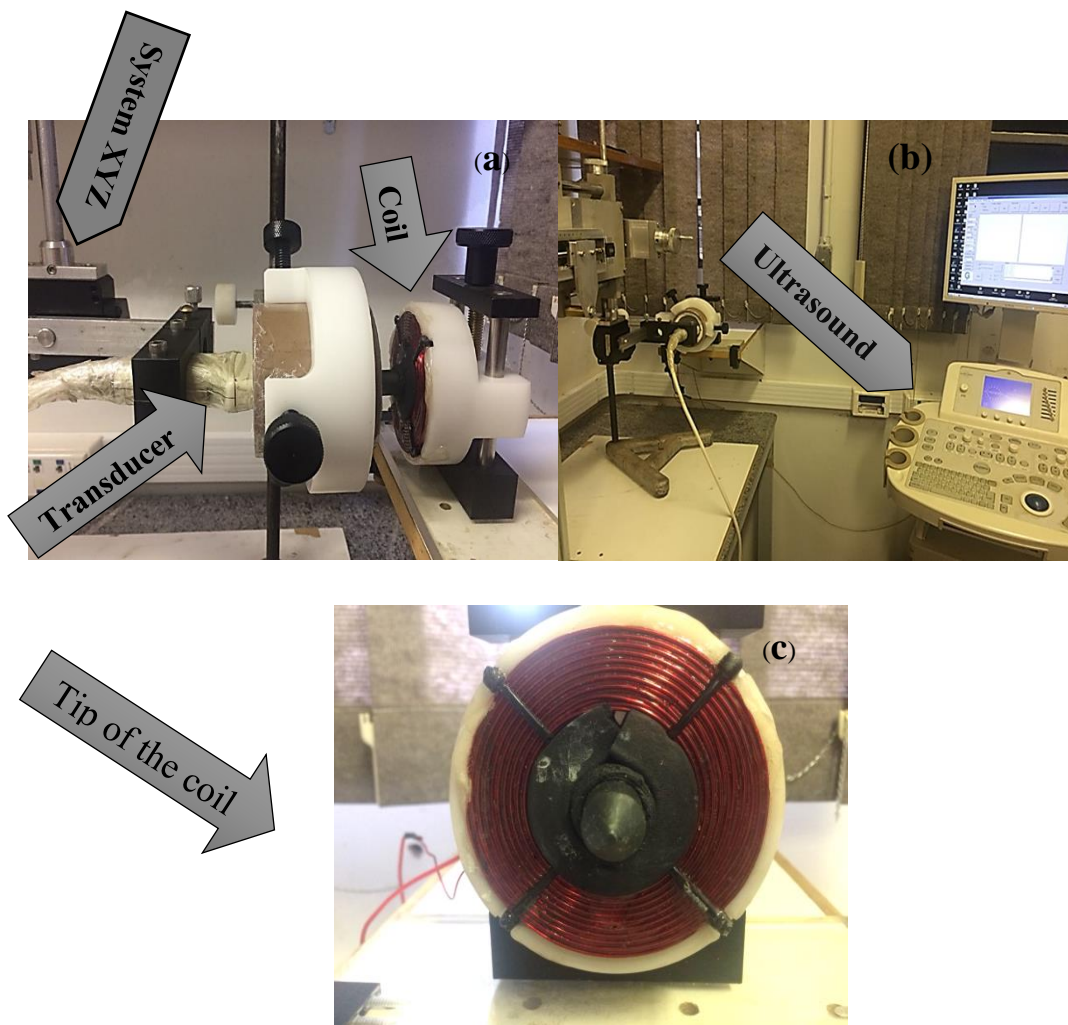


Figure 2.1: Image of the experimental system (a and b). A ferrite core is included in the center of a coil to enhance and focus the magnetic field gradient (c).

A schematic of the experimental setup is illustrated In Figure 2.2.

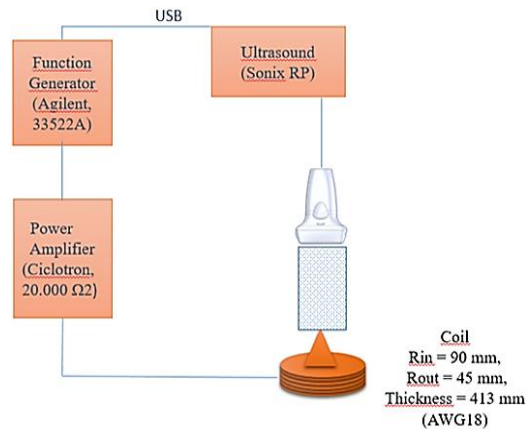


Figure 2.2: Schematic depiction of the experimental setup used to perform the measurements.

## 2.2. The magnetic field

A gaussimeter (TMAG\_IT, Globalmag) with a Hall sensor and an oscilloscope (Agilent Technologies InfiniiVision Mso7b4 B Mixed signal, 1 GHz, 4GSA/S) were used to observe the profile of the magnetic field respect to the tip of the coil. The current on the coil was kept fixed in 2A. Meanwhile, the distance of the gaussimeter was changed from the center of the coil (2 mm - 20 mm). The first distance was considered 2 mm from the tip of the magnetic field concentrator to the surface of phantom (where the surface of inclusion was positioned).

## 2.3. Magnetic nanoparticles ( $Fe_3O_4$ )

All used magnetic nanoparticles ( $Fe_3O_4$ ) were superparamagnetic with different average sizes ranging from 7.9 to 25 nm and different coating materials such as natural rubber latex (NRL) and Polyvinylpyrrolidone (PVP). The saturation magnetization of MNPs changes based on the core size, size distribution and modified surface of MNPs. The properties of superparamagnetic nanoparticles that were used is given in Table 2.2.

The magnetic nanoparticle 1 was purchased from Houston, TX, USA, nanoparticle 2 was made in our lab (GIIMUS, Ribeirao Preto, USP), and magnetic nanoparticles 3-7 (MNps 3-7) prepared in the biomagnetism lab (Ribeirao Preto, USP). Samples 5 and 6 were prepared using 100 and 800  $\mu$ L of latex and they were named MNPs-100NRL and MNPs-800NRL respectively. MNPs-100NRL has thin shell of NRL while MNPs-800NRL has thick shell of NRL because of using high concentration of NRL. NRL has high molecular weight and magnetic saturation of MNPs was measured based on the mass of magnetic nanoparticles, so it is important to know the mass of latex that used for each sample of 5 and 6. By calculating

and subtracting the mass of NRL from the total mass (NRL+ MNPs) of each sample the mass of pure magnetic nanoparticles (MNPs) can be calculated.

It can be seen (Table 2.2) values of magnetization saturation for nanoparticles 5 and 6.

Table 2.2: The properties of superparamagnetic nanoparticles used in the phantoms.

<b>Nanoparticles (Fe<sub>3</sub>O<sub>4</sub>)</b>	<b>Size (nm)</b>	<b>Magnetic saturation (emu/g)</b>	<b>Method</b>	<b>Cover</b>
<b>Magnetic nanoparticles 1 (MNPs1)</b>	25	62	Commercial	Polyvinylpyrrolidone (PVP)
<b>Magnetic nanoparticles 2 (MNPs2)</b>	20	70	Co-precipitation	Without cover
<b>Magnetic nanoparticles 3 (MNPs 3)</b>	12.5	70	Co-precipitation	Without cover
<b>Magnetic nanoparticles 4 (MNPs 4)</b>	12±4.17	57	Co-precipitation	Without cover
<b>Magnetic nanoparticles 5 (MNPs 5)</b>	13±2.8	85	Co-precipitation	100NRL (thin shell)
<b>Magnetic nanoparticles 6 (MNPs 6)</b>	7.9±1.5	119	Co-precipitation	800NRL (thick shell)

#### ***2.4. Tissue mimicking phantom***

To perform the measurements for the mentioned setup, variation of different sizes and shapes for the phantom and inclusion were tested and classified as follows. As the first experiment, a homogenous phantom was made to test the setup. The same types of phantom was prepared in our group in 2015 [102]. In this work, we used a lower concentration of superparamagnetic particles and phantoms (was included an inclusion, with different sizes and

shapes) to investigate the optimized results for SDMMUS measurements. This new method has a potential for clinical application. In this case, a low concentration of iron oxide nanoparticles is needed. The phantoms were prepared with gelatin tissue mimicking phantom for the homogenous ones, while those contained the inclusion were mixed with glass beads and agar.

#### ***2.4.1. Gelatin tissue mimicking phantom***

The tissue mimicking phantom was made with Bloom 250 animal gelatin (bovine), dissolved in deionized water with resistivity of 18.2 M $\Omega$ .cm at 25°C and heated to 70°C to obtain a homogeneous solution and release trapped gases into the solution [103]. To measure the temperature of the solution a digital thermometer Incoterm, Brazil, with temperature of 50 °C to +300 °C, was used continuously until reaching to 70 ° C. For the process of dilution, a heating system model 752A (manufacturer Fisatom, São Paulo, Brazil) and a backer with water, gelatin powder and magnetic stirrer were used. Magnetic mixer is used to spin quickly the solution to effect the mixing and homogeneous. After reaching the temperature to 70 ° C the stirrer was removed. Then, solution was kept in room temperature and mixed slowly to decrease the temperature to 50° C and continued the mixing to homogenize. Soft movements are necessary through mixing to avoid air bubbles for the solution. Therefore, magnetic nanoparticles were added into the solution at 50°C. After the temperature of the mixture reached 40° C, the 5% of the total mass of gelatin was added as a formaldehyde value. Formaldehyde is an anti-bactericidal agent that improve long-term stability of the phantom in addition to increase the melting point and the modulus of the elasticity [104]. While the solution is in liquid state and reach 35° C the mixture was poured into a desired mold that was attached to a motorized system. This system regulates the velocity and applies a rotational motion at 3 rpm for 24 uninterrupted hours within a refrigerator. This rotation is necessary to keep uniform distribution of nanoparticles within the phantom.

To backscatter of the ultrasound wave we used glass beads with diameter less than 37  $\mu$ m in the third phantom. But, as these particles were heavy they deposited on the surface of the inclusion and created a border, this scatter was replaced by the agar gelatin (Agar Bacteriologic CAT. RM026 from the company of HIMEDIA).

Therefore, to make the agar phantoms, the solution was heated until reach 90° C for 4 hours to be completely free of microbubbles and get homogeneous. This solution also was rested in room temperature until reaching 35 °C and then poured into a cylinder mold where the inclusion was positioned in the bottom of it. Finally, the phantom was kept in the refrigerator

again for 24 more. To sum up, 13 phantoms prepared with different shapes as well as different concentration of MNPs which have some specific characteristics as follow:

***The first phantom (P1):*** A gelatin tissue mimicking homogeneous phantom made with 4% of gelatin and 4% concentration of magnetic nanoparticles ( $\text{Fe}_3\text{O}_4$ ). A concentration of 5 % (0.84ml) of formaldehyde was added to the solution at 40° C. The used superparamagnetic nanoparticles were commercial (Nanostructured & Amorphous Materials Inc., Houston, TX, USA) and with the size 25 nm, coated with 1% PVP (polyvinylpyrrolidone) and magnetic saturation of 62emu/g. After preparation, the solution put into the acrylic cube with dimension of 75x75x75  $\text{mm}^3$  and attached to a rotational system, Figure 2.3. This phantom was prepared using the same nanoparticle as phantom prepared in our group in 2015. But here this phantom was considered as the first experiment to test the setup.

***The second phantom (P2):*** A gelatin tissue mimicking homogeneous phantom made with 4% of gelatin and 0.5% concentration of iron oxide nanoparticles ( $\text{Fe}_3\text{O}_4$ ). The same nanoparticles used (sample1) in this phantom. The solution was poured in the cylinder mold with dimension of 60x60  $\text{mm}^2$  and 5% (0.34 ml) of formaldehyde was added to the solution at 40° C. In both phantoms (P1 and P2) were used a high concentration of magnetic nanoparticles which are not appropriated for the biomedical application.

***The third phantom (P3):*** In this part, there are two molds: a cylindrical phantom with a spherical inclusion, Figure 2.4 (a). The procedure to prepare the phantom was the same as before but using gelatin tissue mimicking phantoms with glass beads. The inclusion is spherical with diameter of 1.5 cm, with 1% concentration of magnetic nanoparticles ( $\text{Fe}_3\text{O}_4$ ), the same one used for the phantom P1 and P2 and 5% (0.0035 ml) of formaldehyde. 5% of formaldehyde (0.34 ml) and 0.5% of glass beads were used in this phantom (cylindrical shape with diameter of 60 cm and height of 60 cm). This type of phantom with spherical inclusion did not provide good results as is shown in the next chapter. Finally, after trying some trials the optimized phantom was chosen as described in the fourth phantom.

***The fourth phantom (P4):*** This phantom was made using the same procedure as aforementioned in phantom 3. While the shape of inclusion was changed to the cylinder mold with diameter of 20 and height of 20 mm, Figure 2.4 (b), the phantom background shape and size were the same as the phantom 3 (Tissue mimicking phantom was prepared with 4% of gelatin, 2% of Agar replaced instead of glass beads). The inclusion was homogeneously labeled with 1% of magnetic nanoparticles. The used nanoparticles for this phantom contained 5 groups which is shown in Table 1.1 MNPs 1-5. Moreover, the 0.3% of iron oxide nanoparticles

of group 4 is used to check the displacement profile and the shear wave propagation. Furthermore, four more concentration of MNPs-800NRL such as 0.10%, 0.20%, 0.30%, and 0.70% were used to investigate the limitation in SDMMUS modality.

The phantom was kept for 2 days in the refrigerator before performing the measurements, to stabilize its structure (Figure 2.5). B-mode ultrasound image was obtained for all phantoms to identify the structures that could improve measurements as bubbles or accumulation of ferromagnetic material in any region. If phantom faced these problems, it was discarded a chemical waste. For each sample two phantoms were prepared with the same characteristics for doing measurements.

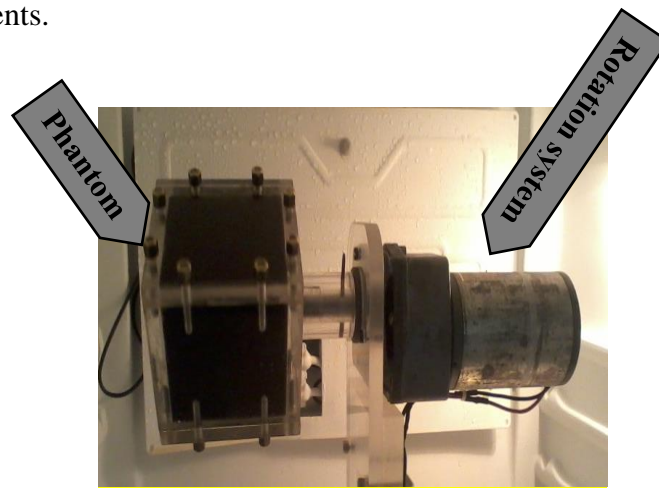


Figure 2.3: The rotation system to homogenize the phantom.

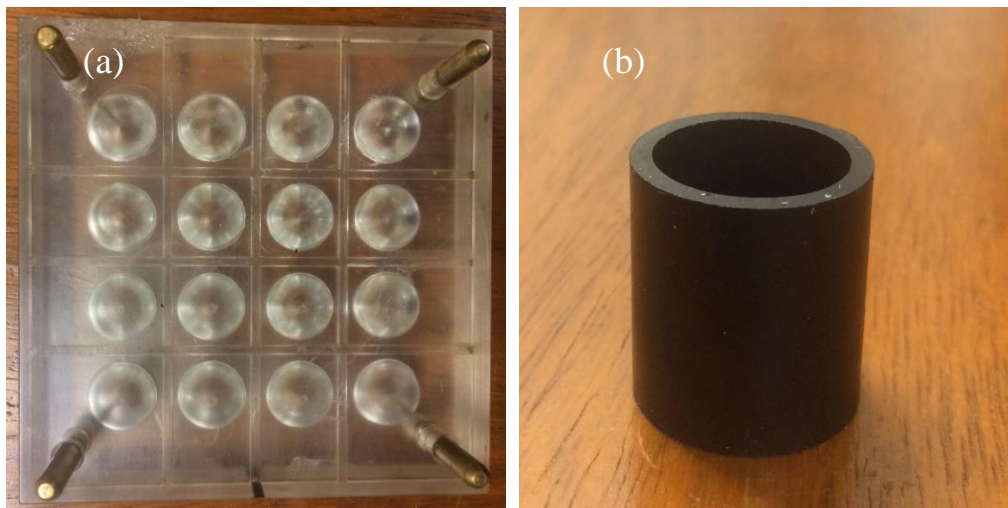


Figure 2.4: Mimicking phantom mold with: (a) spherical and (b) cylindrical inclusion shape.

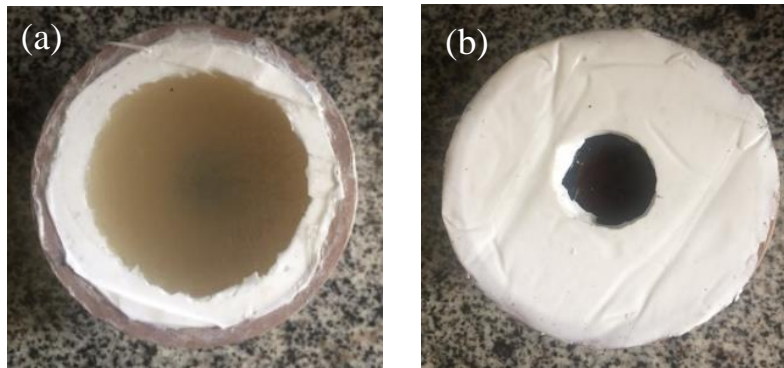


Figure 2.5: The cylindrical phantom that a cylinder inclusion is embedded in.

## 2.5. Ultrasound system

The RF data was acquired using a programmable ultrasound equipment Sonix RP (Ultrasonix, DK, Boston, Massachusetts, USA). The specifications of Sonix RP are listed in Table 2.3, while the characteristics of the linear transducer (L14-5/38) coupled to the Sonix RP are listed in Table 2.4.

Table 2.3. Ultrasound system specifications

<b>Model</b>	<b>Sonix RP</b>
<b>Transducer</b>	128 Elements (Linear)
<b>Chanals (TX)</b>	128
<b>Chanals (RX)</b>	32
<b>Max sampling frequency</b>	40 MHz
<b>ADC</b>	10-bit
<b>operational system</b>	Windows XP 32-bits

Table 2.4: Characteristics of the used transducers coupled to Sonix RP.

<b>Elements</b>	<b>128</b>
<b>Model</b>	(L14-5 / 38)
<b>Bandwidth</b>	14-5 MHz
<b>Pitch</b>	0.30 mm
<b>Depth</b>	20 mm up to 90 mm

To acquire RF data, the Sonix RP was set to run a MMUS dedicated platform that enables us to acquire MMUS data via graphical user interface [101]. This platform automates a MMUS acquisition system by controlling a function generator, which syncs ultrasound acquisition with magnetic excitation, and storing RF data, as can be seen in Figure 2.6.

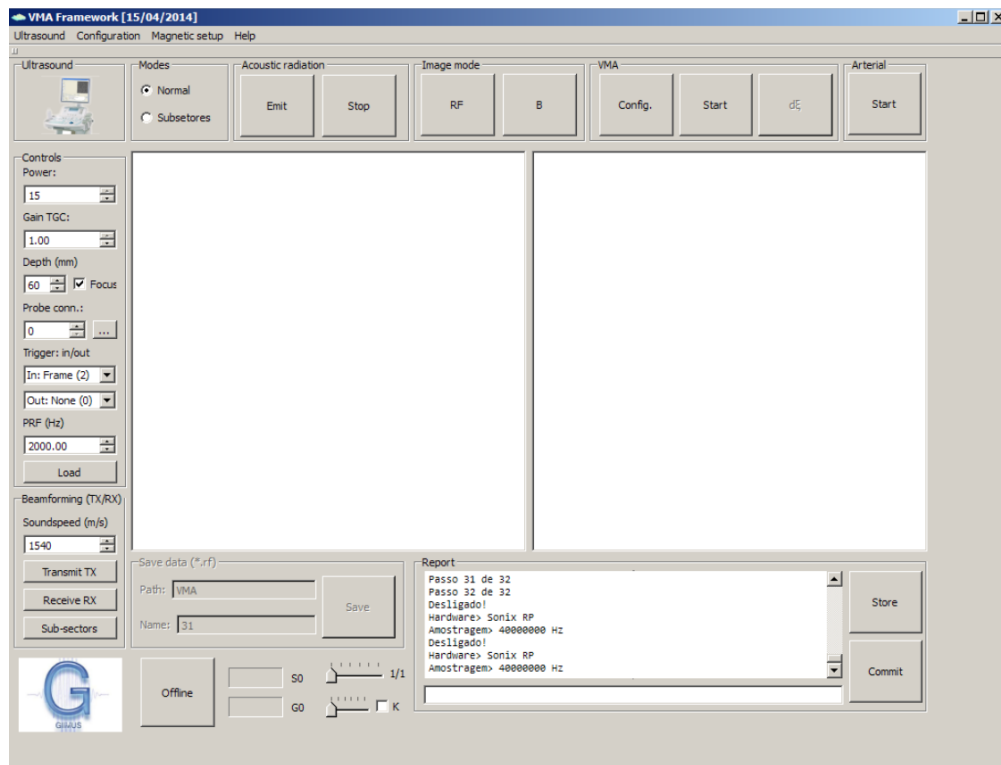


Figure 2.6: MMUS platform user interface.

The configuration was performed by choosing a commonly used set of ultrasound imaging-related parameters such as depth and sound speed. To acquire MMUS data, it is required the configuration of an MMUS pulse sequence that has a high framerate (described in the section 2.5.1) and a magnetic waveform; we configured an MMUS pulse sequence by considering a framerate of 2000 Hz and a sine magnetic excitation waveform to driven the excitation coil (see section 2.1). In Figure 2.7 parameteres including waveform of the excitation (pulse or sinousidal), the frequency, amplitude, and the number of cycles are adjustable.

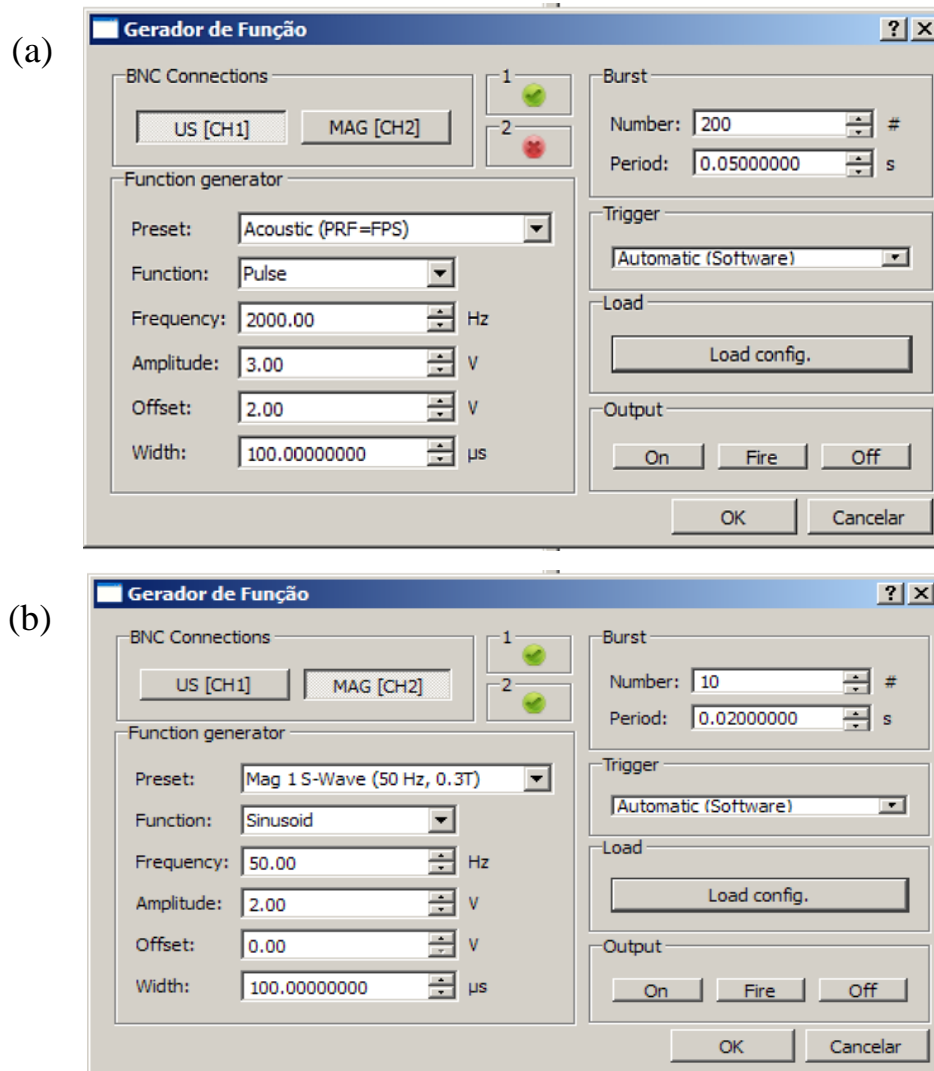


Figure 2.7: The user interfaces of an MMUS timing sequence. (a) Ultrasound acquisition and (b) Magnetic excitation.

### 2.5.1. High framerate

To obtain a high framerate, the MMUS platform generates a high framerate ultrasound beamforming time aligned with the magnetic excitation, it acquires data by dividing the transducer into subsectors, for instance a subsector of the transducer with 4 activated elements presents a frame rate 8-fold higher than a subsector with a size of 32 activated elements, each subsector is acquired for a fixed time that is big enough to track the displacements induced by the magnetic excitation [101].

### 2.6. Particle displacement

The particle displacement induced by the magnetic force is in the order of microns. Therefore, it is needed to use a tracking algorithm that compare ultrasound signals to obtain the particle displacement. For instance, consider two ultrasound RF signals  $s_1$  and  $s_2$ , that are

obtained before and after magnetic excitation, respectively. A comparison between those two signals should provide the particle displacement if it is possible to track a time delay between  $s_1$  and  $s_2$ . There are many methods capable of tracking time delays between ultrasound RF signals, one of them uses a cross-correlation-based algorithm [101], which is applied first to obtain an auto-correlation (AC):

$$s_1 \times s_1 = R s_1 s_1 \quad (1.26)$$

And then, cross-correlation (XC):

$$s_1 \times s_2 = R s_1 s_2 \quad (1.27)$$

$R$  is a vector that corresponds to the cross correlation of those two discrete signals, which operates  $s_1$  and  $s_2$  as matrices.

It is computationally efficient to obtain AC and XC using a Fourier transform:

$$AC = F^{-1} [F(s_1) \times F(s_1)^*] \quad XC = F^{-1} [F(s_1) \times F(s_2)^*] \quad (1.28)$$

The time delay ( $\tau$ ) is obtained comparing the time location of the peaks of maximum correlation of  $R s_1 s_1$  and  $R s_1 s_2$ , which is given in units of time as ( $\tau_{\text{sec}}$ ) is,  $\tau_{\text{sec}} = \frac{\tau}{f_s}$ , where  $f_s$  is the sampling rate of the ultrasound RF signal. Therefore, a particule displacement  $u$  is obtained:

$$u = \frac{c_s \tau_{\text{sec}}}{2} \quad (1.29)$$

Usually, the time location of the peak of maximum correlation is biased by noise or limited sampling frequency; therefore a polynomial fit is then applied to reduce bias that could affect the location of the peak of maximum correlation [101]. In summary, a tracking algorithm is applied to a RF map to obtain a displacement map that is given in microns ( $\mu\text{m}$ ). As long as we have sufficient framerate, the shear wave can be mapped, and its propagation through the medium is analyzed to obtain the shear wave velocity:

$$c_{sw} = \frac{u}{t} \quad (1.30)$$

The aforementioned 1-D signal algorithm can be applied in a 2-D map, where the cross-correlation is applied over pairs of maps indexed by the variable  $t$ , for example, if we take the

$t = 1$  and  $t + 1 = 2$  the next pair of cross-correlation is then  $t = 2$  and  $t + 1 = 3$ , resulting in a particle velocity 2-D map (Fig 2.8)[101].

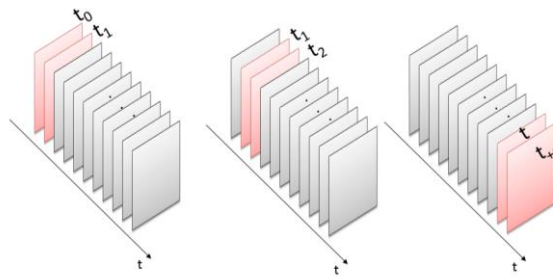
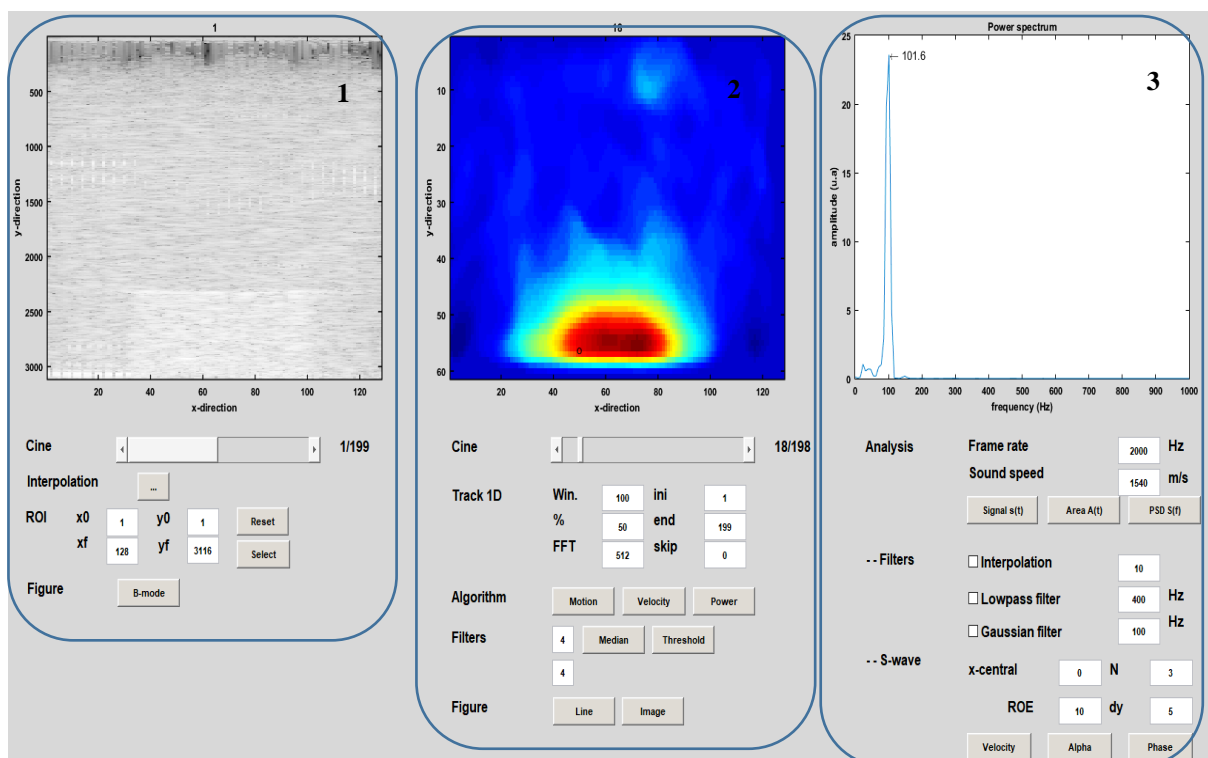


Figure 2.8: 2-D particle velocity map [101].

This method has a particular set of parameters that can be configured to enhance the accuracy; Since it is a 1-D algorithm applied over a 2-D RF map, lines of map are processed along depth by selecting a rectangular window (with a size of 1.0 mm), which is overlapped by 70% with the next window to increase the spatial resolution in depth and accuracy of displacement. All this algorithm is already implemented in the MMUS platform [101] and the user graphic interface is depicted below (Figure 2.9).



The MMUS platform provides three main parts. 1) Generates a B-mode image, 2) generates a MMUS displacement image, which tracks shear waves movement, and 3) analyzes shear wave signal by assessing amplitude and frequency of displacement signal. As explained previously, the framerate is 2 kHz and soundspeed is 1540 m/s. The average of displacement was evaluated in the region of interest (ROI) with a size of  $10 \times 10 \text{ mm}^2$  from the face of the phantom and 3 mm far the tip of the core. it can be noticed that the magnetic NPs movement is tracked by MMUS platform (Figure 2.10).

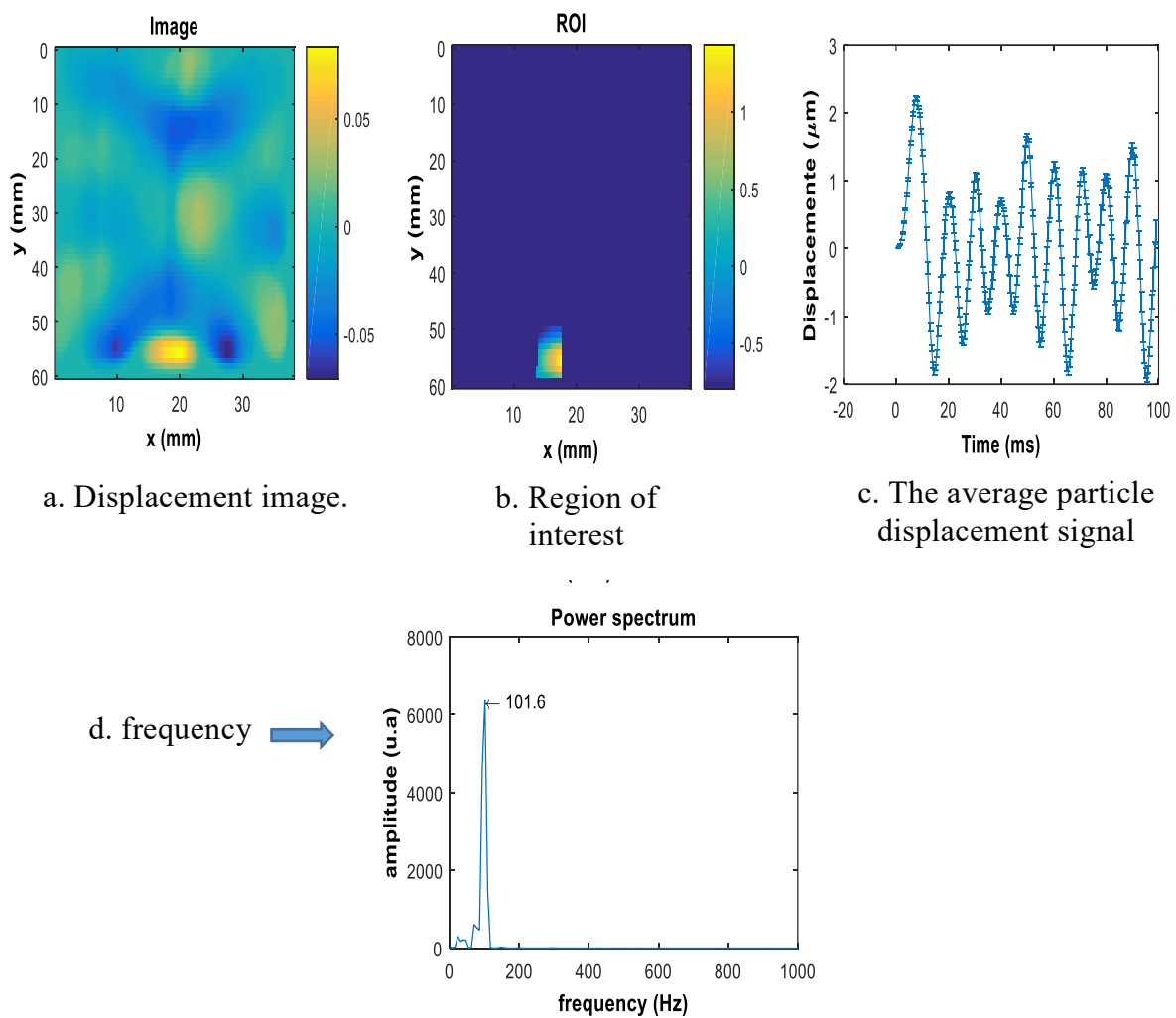


Figure 2.10: Analysis of shear wave signal. (a) Displacement image, (b) region of interest selected to obtain a spatial average of the particle displacement signal, (c) the average particle displacement signal and its (d) frequency spectrum.

## 2.7. Shear wave velocity and viscoelastic parameters

The shear wave velocity can be obtained by tracking the peaks of maximum amplitude of the shear wave signal during its propagation through depth. As can be seen in Fig. 2.11, the shear wave signal's peak of maximum amplitude decreases its value when analyzed at three different depths 51 mm, 46 mm, and 41mm. As long as it is possible to track the peak of maximum intensity, a time to peak (TTP) algorithm was used to assess the position of the shear wave as a function of time [105]. The normalized amplitude is obtained by normalizing the shear wave signal with the maximum amplitude within the analysis window. This normalized amplitude decreases because of the attenuation caused by the phantom viscoelastic properties.

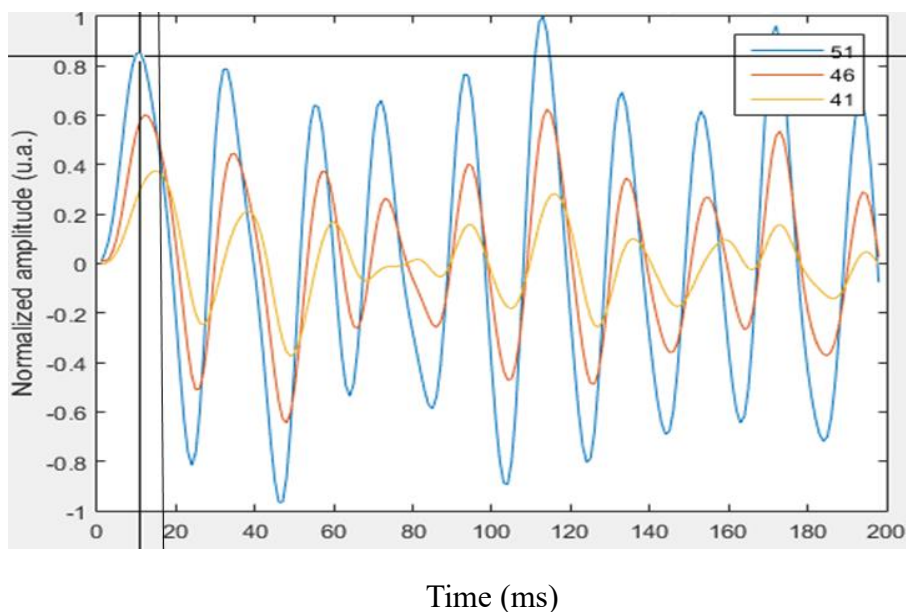


Figure 2.11: The shear wave analysis is performed via the window of analysis of MMUS platform, it shows three shear wave signals at 51 mm, 46 mm, and 41mm depths.

To obtain the shear wave velocity, TTP algorithm was used to correlate at least two shear wave signals; the position of the peak of maximum amplitude of the shear wave as a function of time is given, and then a linear function fits these values. The shear wave velocity was obtained by considering the slope of the linear function that fits TTP data (see the purple circle in Figure 2.12).

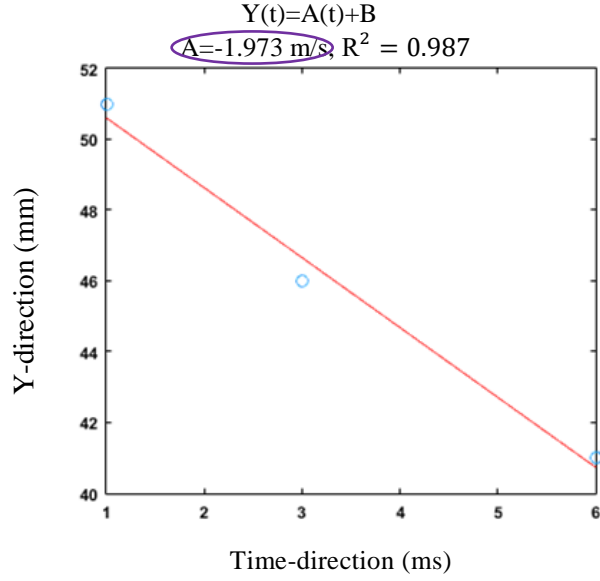


Figure 2.12: The time to peak algorithm is used to obtain shear wave peak position as a function of time, and then a linear fitting is applied obtain the shear wave velocity.

The shear wave velocity was obtained by using excitation different frequencies. The frequency range was set to vary from 50 - 250 Hz using steps of 50 Hz. Assuming Kelvin-Voigt model for a viscoelastic medium with mass density  $\rho$ , the shear wave velocity  $c_s$  is given as:

$$c_s = \sqrt{\frac{2(\mu_1^2 + \omega_s^2 \mu_2^2)}{\rho \left( \mu_1 + \left( \sqrt{\mu_1^2 + \omega_s^2 \mu_2^2} \right) \right)}} \quad (1.31)$$

where  $\omega_s$  is the shear wave frequency, and the shear elasticity and viscosity are  $\mu_1$  and  $\mu_2$ , respectively [29].

To obtain  $\mu_1$  and  $\mu_2$ , the Levenberg-Marquardt algorithm [106] was applied to perform a non-linear adjustment considering  $\omega_s$  and  $c_s$ . This algorithm was implemented in Matlab [107].

### 3. Results and Discussion

#### 3.1. Analysis of magnetic field of excitation coil

To observe the effect of magnetic field by changing the distance of gaussimeter regard to the coil, some measurements were done as discussed in chapter 2.2. As can be observed in the Figure 3.1 (a), the distance of 3 mm depicts the magnetic field of 0.14 T. The variation of amplitude of magnetic field for various distances is reported (Figure 3.1 (b)). Clearly, increasing the distance of the gaussimeter to the coil will decrease the amplitude of the magnetic field. For example, from 10 mm of the tip of the coil the Magnetic Field is 0.05 T. The highest magnetic field (0.16 T) was observed for the closest distance of 2 mm, in Figure (3.1 (b)).

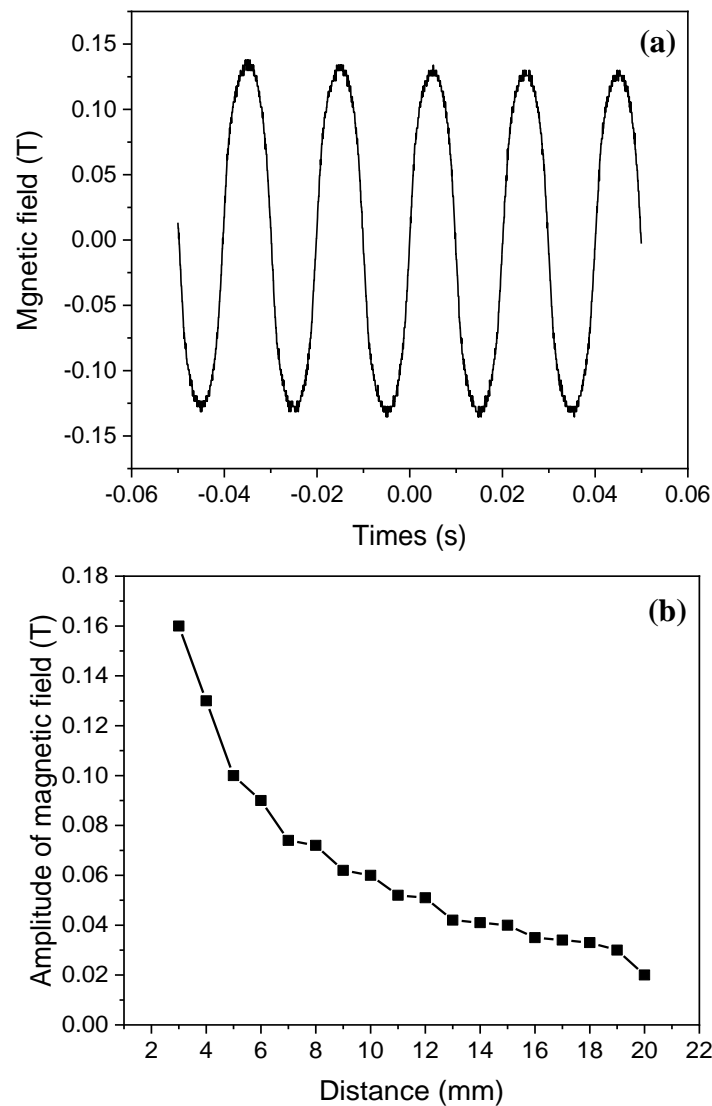


Figure 3.1: The profile of the magnetic field with respect to the tip of the coil. a) Oscillating magnetic field 3 mm far from the tip with excitation frequency of 50 Hz; b) Amplitude the magnetic field for different distances from tip.

### ***3.2 Evaluation of acquisition system***

A fixed magnetic field of about 0.16 T at a distance of 2 mm far from the tip of the ferrite core was considered. The propagation of the shear wave was achieved by applying this field and distance for all phantoms. Based on these measurements, up to 4 mm away from the excitation region can be considered as a critical area. The variation in the magnetic field is mainly due to the change of resistance in the coil originating from the variation of the frequency of the applied signal [91]. 10 cycles were used with a range of frequencies from 50-250 Hz during the analyzes of the magnetic field generation by the coil.

### ***3.3 Evaluating phantoms for SDMMUS imaging***

Figures 3.2 (a) and (b) show the processed signal of the shear wave of magneto motive ultrasound, (the processing method explained in section 2.6), for magnetic excitation of 50 Hz.

As discussed previously in the second chapter, various phantoms were prepared with different superparamagnetic nanoparticles with different saturation magnetization. In this thesis, first homogenous phantom (**p1**) was made with high concentration of iron oxide MNPs1, shows that these nanoparticles are suitable for this modality using the same methodology as in [108]. As can be seen, images of shear wave propagation have a high resolution showing the feasibility of the method using commercial magnetic nanoparticles (Figure 3.2).

In Figure 3.3, the amplitude of the shear wave propagating through the phantom in three different depths are shown. In this Figure, the blue line is considered as the first depth at 66 mm away from the ultrasound transducer. The two other lines are deeper depths of further. As it was expected, the amplitude reduced because of the signal attenuation in the medium.

As aforementioned in chapter 1.7 the frequency spectrum of magnetic nanoparticles should be twice larger than excitation frequency (50 Hz) which depicted below in Figure 3.3. The frequency of magnetic nanoparticles displacements was seen at 93.8 Hz. This value was already expected as described in the Eq. 1.26, because the magneto motive force created by an alternating magnetic field must be two times larger than the excitation frequency [92]. This can be used as a confirmation that the observed displacement is due to the applied magnetic field.

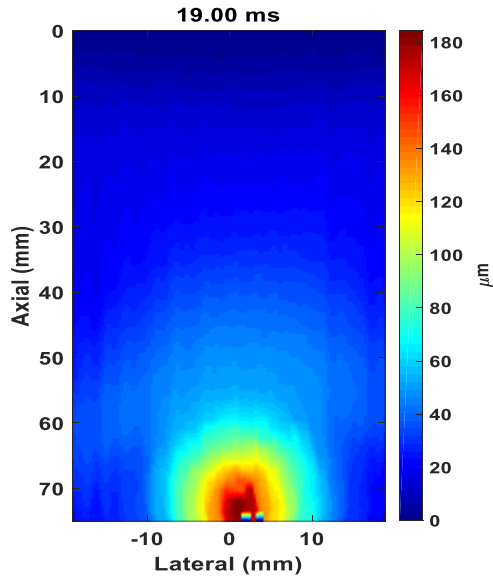


Figure 3.2: Propagation of the shear wave in the phantom with 4% of gelatin and 4% of nanoparticle with magnetic excitation of 50Hz.

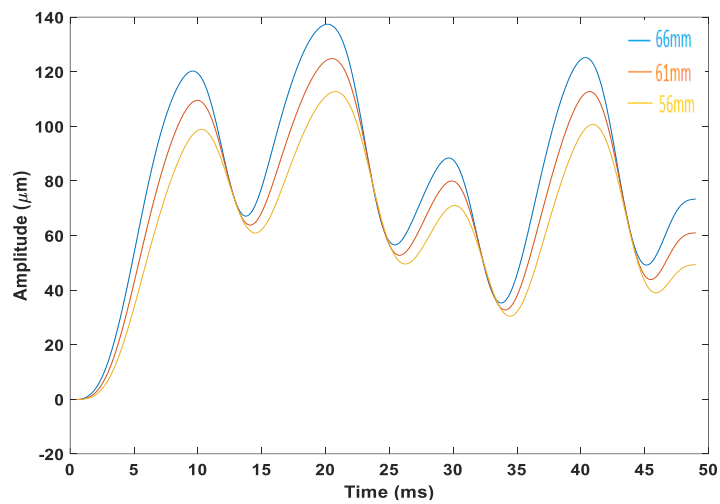


Figure 3.3: Displacement of the shear wave through the phantom for 4% gelatin and 4% concentration of  $\text{Fe}_3\text{O}_4$  in three depths.

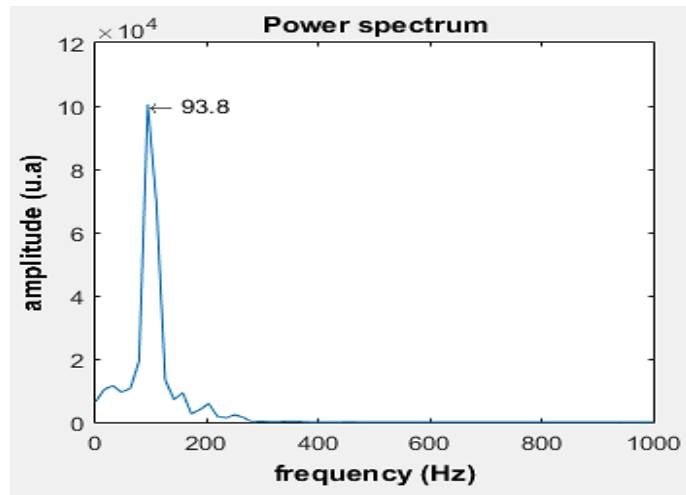


Figure 3.4: Frequency of the magnetic nanoparticles movement

It should be noticed that the maximum mechanical displacement of the medium is near to the region of the magnetic field concentrator, because more intensity is seen in this region. However, the area which is near to the tip of the coil (region of excitation) during the evaluating of the shear wave displacement should not be considered, because of the influence of the excitation and as well as the inertial effect of the movement.

Figures 3.5 and 3.6 show the results for the second homogenous phantom (**p2**) including 0.5% of MNPs. As can be observed, the shear waves are propagating in two different times in Figure 3.5. The frequency of magnetic nanoparticles displacements can be observed below in Figure 3.6.

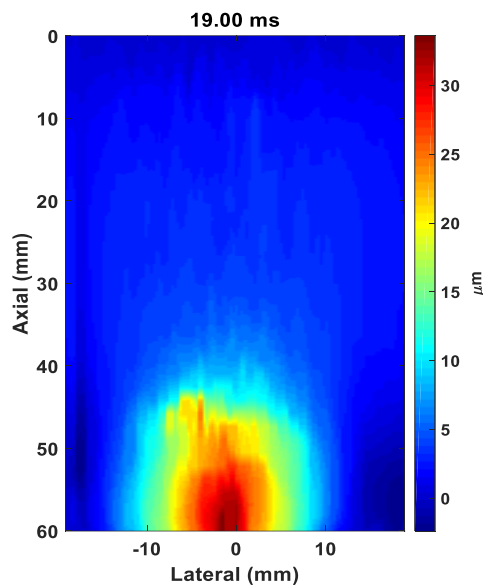


Figure 3.5: Propagation of the shear wave in the phantom with 4% of gelatin and 0.5% of nanoparticle in 19 ms.

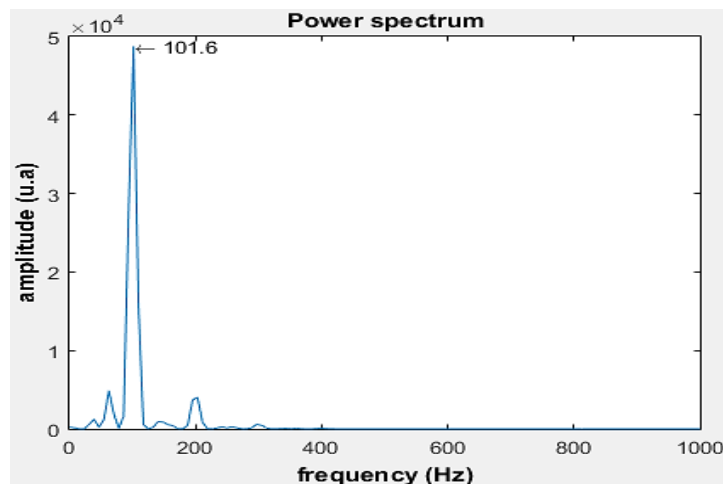


Figure 3.6: The frequency of the magnetic nanoparticles movement.

**The third Phantom (P3):** As can be shown for this phantom (Figure 3.7) the shear wave images did not show a good shear wave because the glass beads precipitated on the surface of inclusion and created a border. Therefore, big reflections were seen in this border and shear wave could not propagate through the phantom, only around the inclusion.

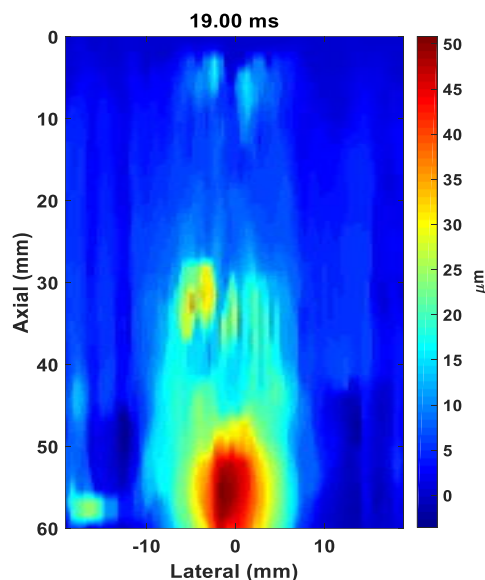


Figure 3.7: Propagation of the shear wave in the phantom with 4% of gelatin and 1% of MNPs 1 as an inclusion in 19 ms.

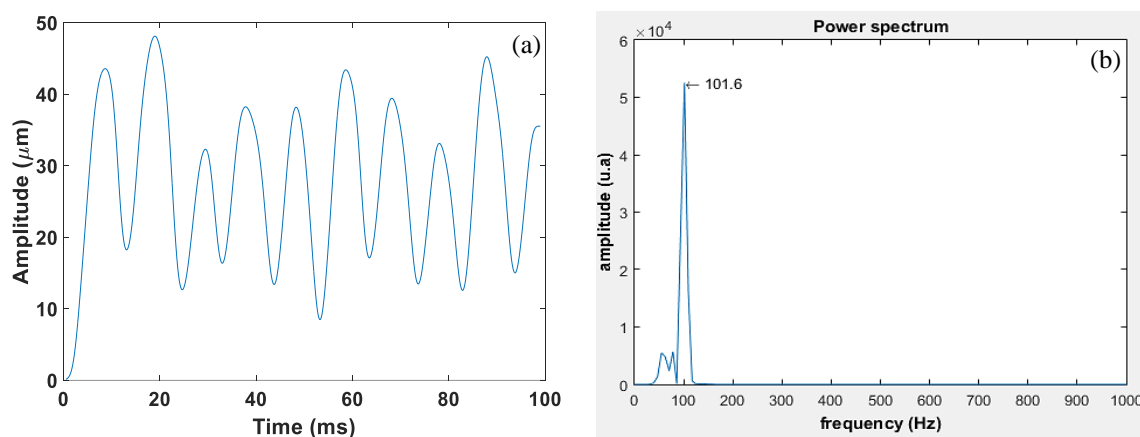


Figure 3.8: a) Displacements due to the shear wave by the gelatin phantom (4%) and 1% concentration of  $\text{Fe}_3\text{O}_4$  (nanoparticles 25 nm) and b) frequency of the magnetic nanoparticles movement.

**The fourth and fifth phantom (P4 and p5):** As it was explained above, the spherical inclusion included glass beads did not depict good results for the shear wave. Therefore, this inclusion was replaced by a cylinder for the other phantoms. The first comparison with a cylinder inclusion was done on the MNPs 2 (size 20 nm), (p4), and the MNPs 3 (size 12.5 nm), (p5). Figure 3.9 shows the magnetization curves for the MNPs 2 (black color) and nanoparticle 3 (red color) both samples have the same saturation magnetization 70 emu/g. In this study, a

specific time, 60 ms was considered for the spectrum of displacements during the time. The aim of the comparison of these two samples was to investigate the influence of size and magnetization on the induced displacement. Shear wave propagation for both phantoms illustrates in Figure 3.10 and 3.11, respectively. Figure 3.12 describes the induced displacements for the fourth (a) and fifth (b) phantoms as well as their magnetic nanoparticles frequency in Figure 3.13.

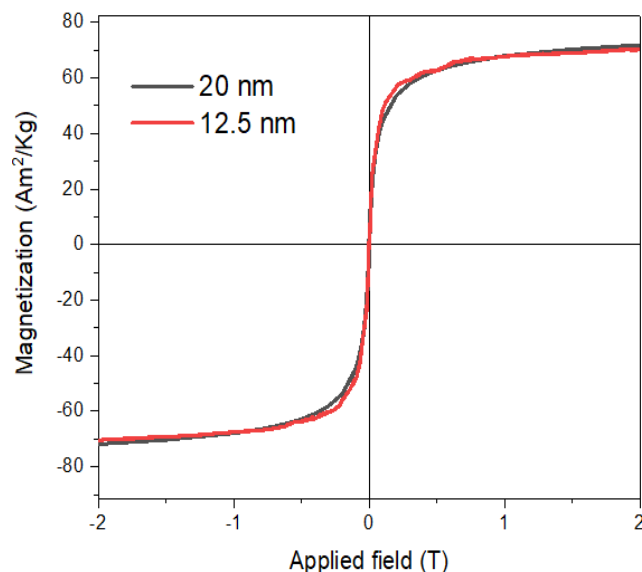


Figure 3.9: Magnetization curves for the MNPs 2 (20 nm) and MNPs 3 (12.5 nm.)

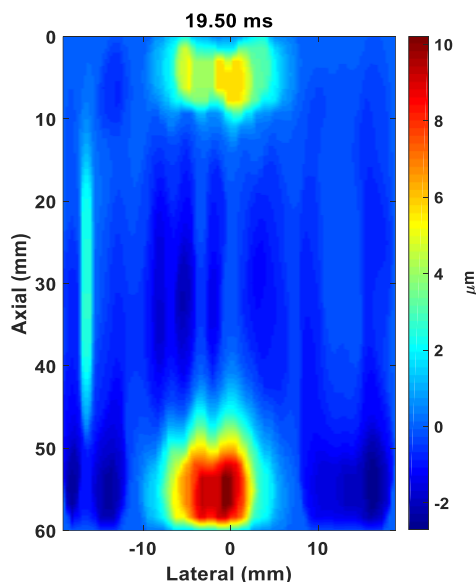


Figure 3.10: Propagation of the shear wave in the phantom with 4% of gelatin and 1% of MNPs 2 (20 nm) as an inclusion.

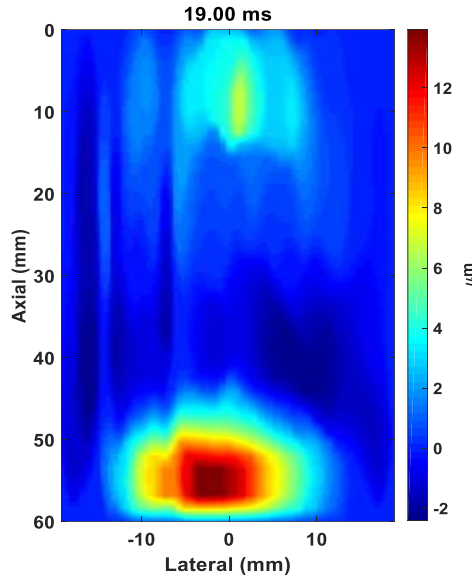


Figure 3.11: Propagation of the shear wave in the gelatin phantom (4%) and 1% of MNPs 3 (12.5 nm) as an inclusion in 19 ms.

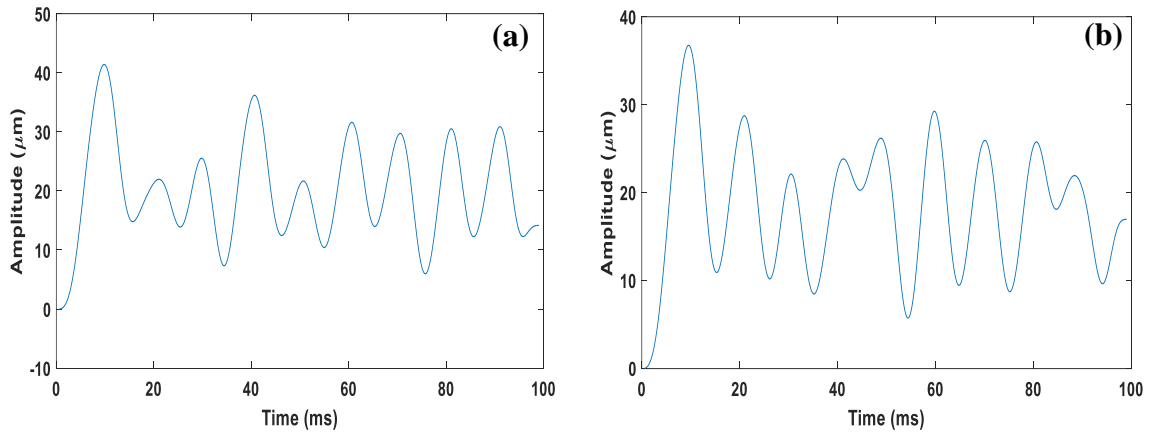


Figure 3.12: Displacements due to the shear wave within the phantom for 4% of gelatin and 1% concentration of nanoparticles (20 nm (a)) and nanoparticles (12.5 nm (b)).

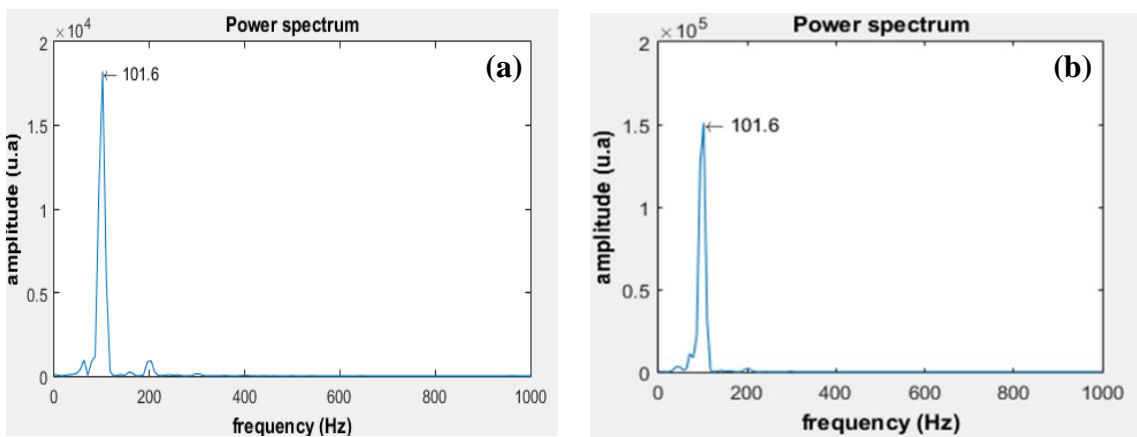


Figure 3.13: The frequency of the magnetic nanoparticles movement for phantom fourth (a) and fifth (b) respectively.

Based on the obtained results (Figure 3.12), the induced displacements for these 2 phantoms (p4 and p5) were  $20 \pm 1.32$  and  $18.2 \pm 1.15$   $\mu\text{m}$  respectively at 50 ms. Although the MNPs 2 (20 nm) has a larger core size than MNPs 3 (12.5 nm) the value of the induced displacement was almost the same because of having the same saturation magnetization. From this comparison can be noticed that the effect of magnetization is higher than size of MNPs. As can be observed in Figure 3.11, there is some reflections at the end of the image namely the bottom of phantom (opposite side of the ROI). This occurs mainly because of the impedance differences between phantoms and air at the border. To remove this effect, we designed a silicon mold and prepared the gelatin based agar phantom inside this mold. As a result, the interface gelatin-air changed to gelatin-silicon, which the latter shows less impedance differences.

Since biological tissue has dispersive property, the shear wave propagation and the induced tissue displacement are frequency dependent [109]. Therefore, for P4 and P5 (Figure 3-14) different values of shear wave velocities were achieved for each frequency response of the medium (50- 250 Hz). After that, the mechanical parameters such as shear elasticity and viscosity were calculated by the Levenberg-Marquardt algorithm [106].

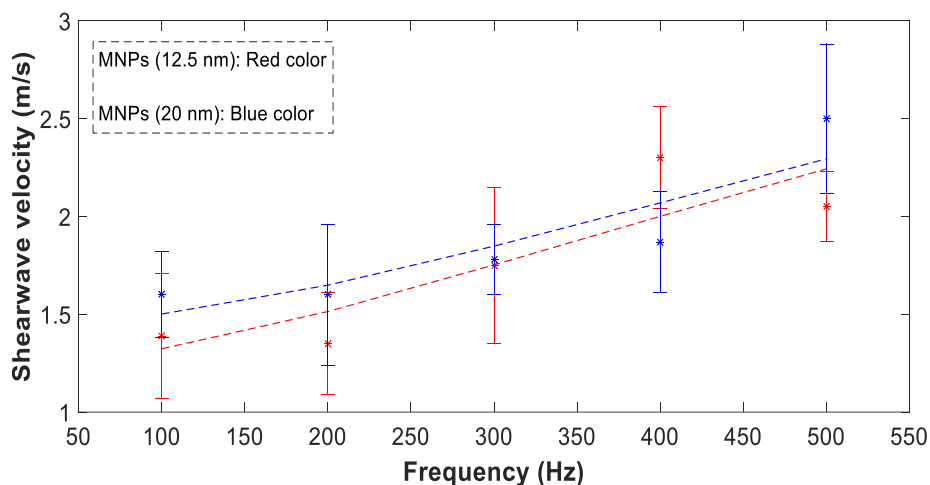


Figure 3.14: Velocities of shear wave versus different frequencies (phantom fourth and fifth).

The acquired values of shear elasticity for fourth and fifth phantom were  $2.08 \pm 0.33$  and  $1.67 \pm 0.26$  kPa for MNPs (20 nm) and (12.5 nm), respectively. The values of shear viscosity were  $1.08 \pm 0.19$  and  $1.034 \pm 0.14$  Pa.s, respectively.

**The sixth-ninth phantoms (P6-9):** For these phantoms MNPs 4, MNPs-100 NRL and MNPs-800NRL were used as an inclusion. Figure 3.15 reports TEM images and histograms of

the size distributions of MNPs and NRL-coated MNPs. Figure 3.16 exhibits the magnetization curves for uncoated MNPs and NRL-coated MNPs considering the mass of iron oxide.

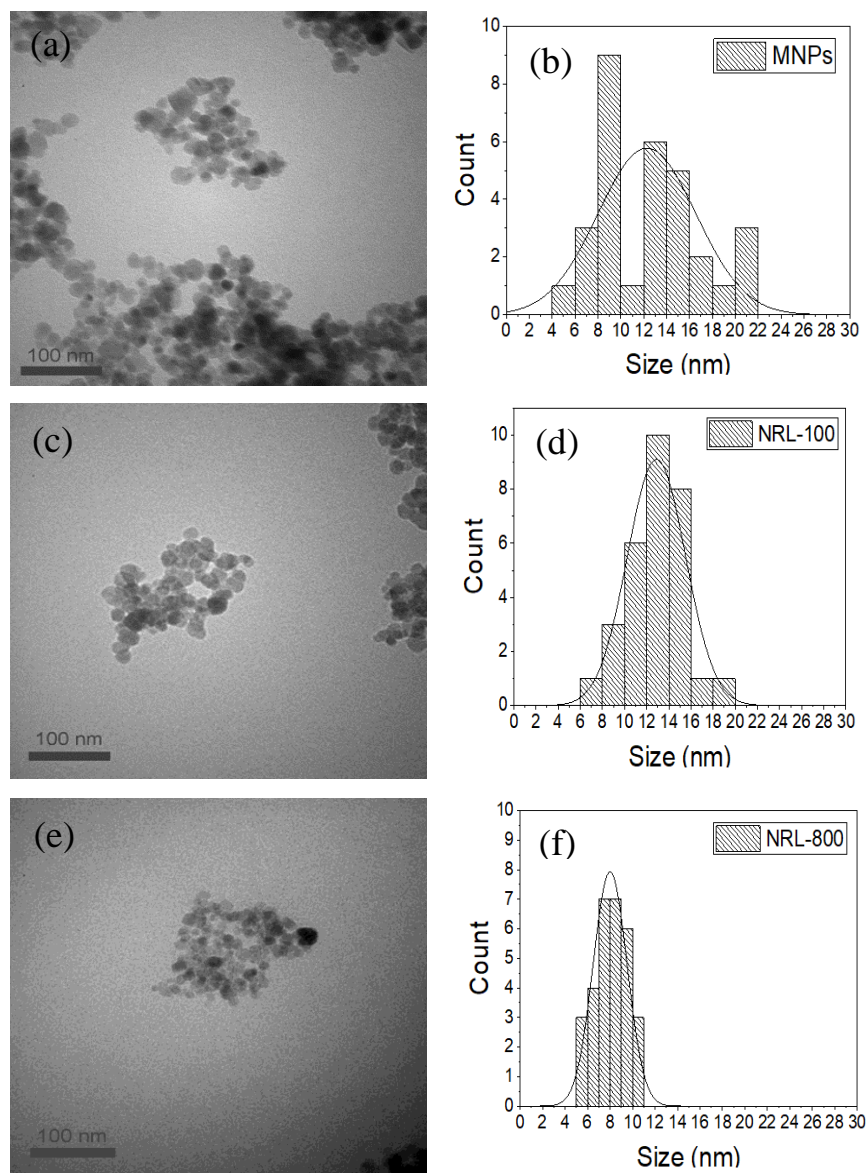


Figure 3.15: TEM images and histograms of the particle size distribution of bare MNPs (a-b) And for 100NRL (c-d) and 800NRL (e-f).

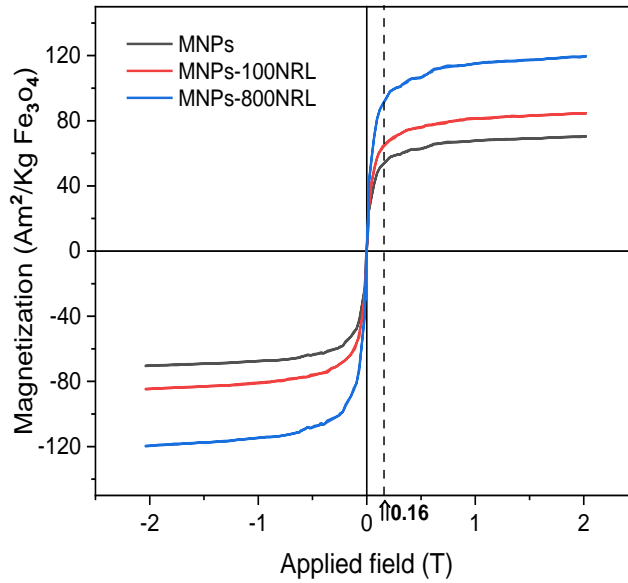


Figure 3.16: Magnetization curves of MNPs and NRL-coated MNPs measured by Hall magnetometer considering only the mass of iron oxide nanoparticles (MNPs).

**In the sixth and seventh phantom (P6 and P7)** MNPs 4 were used as an inclusion 1 % and 0.3% concentration of magnetic nanoparticles respectively. Figure 3.17 demonstrate the shear waves propagating through these phantoms for two different times.

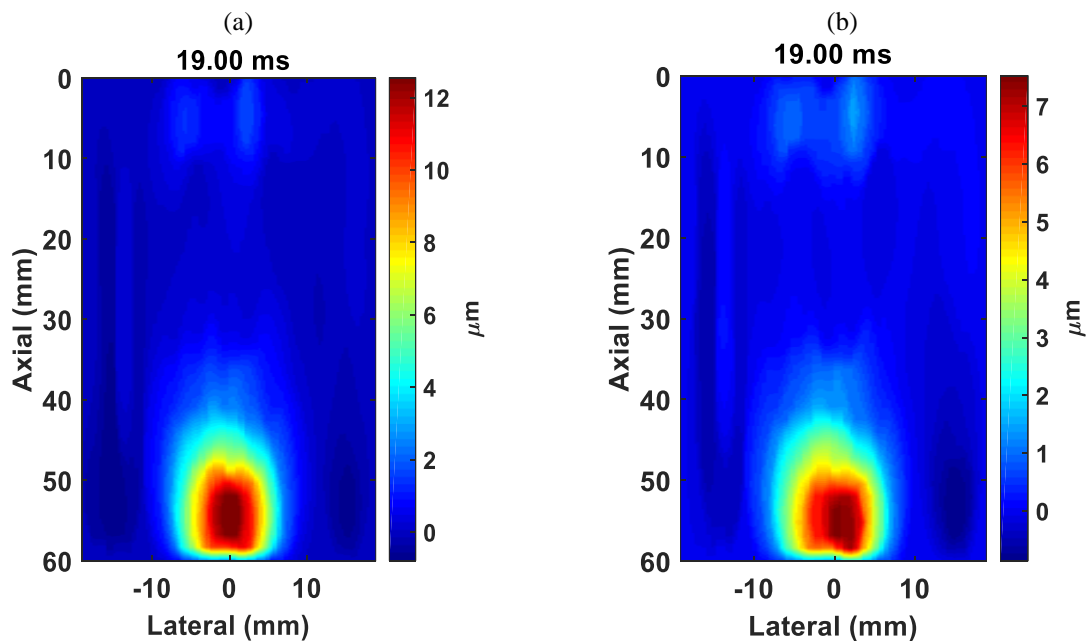


Figure 3.17: Propagation of the shear wave in the phantom seventh with 4% of gelatin for 1% (a) and 0.3% (b) of MNPs 3 as an inclusion in 19 ms.

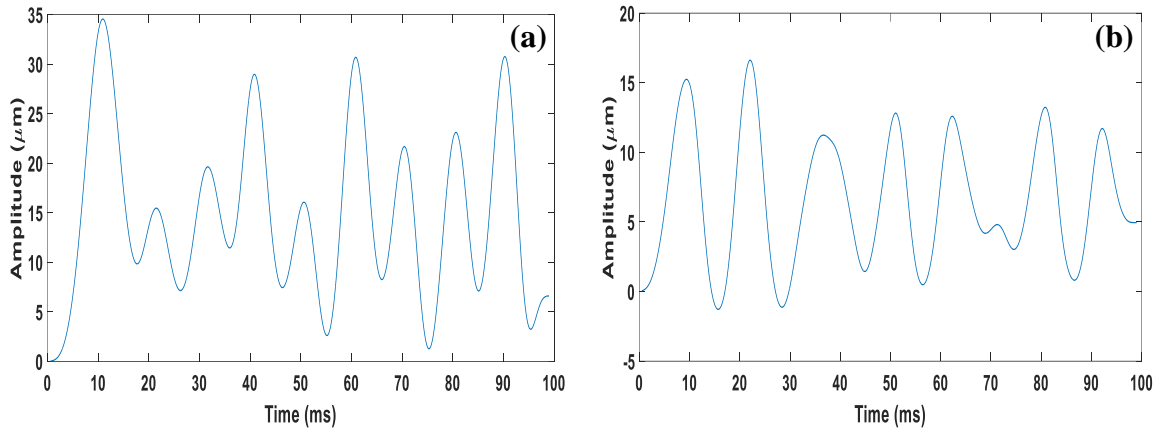


Figure 3.18: Displacement due to the shear wave within the phantom (4% gelatin) and 1 % concentration (p6, a) and 0.3% (p7, b) of e MNPs 3 (b).

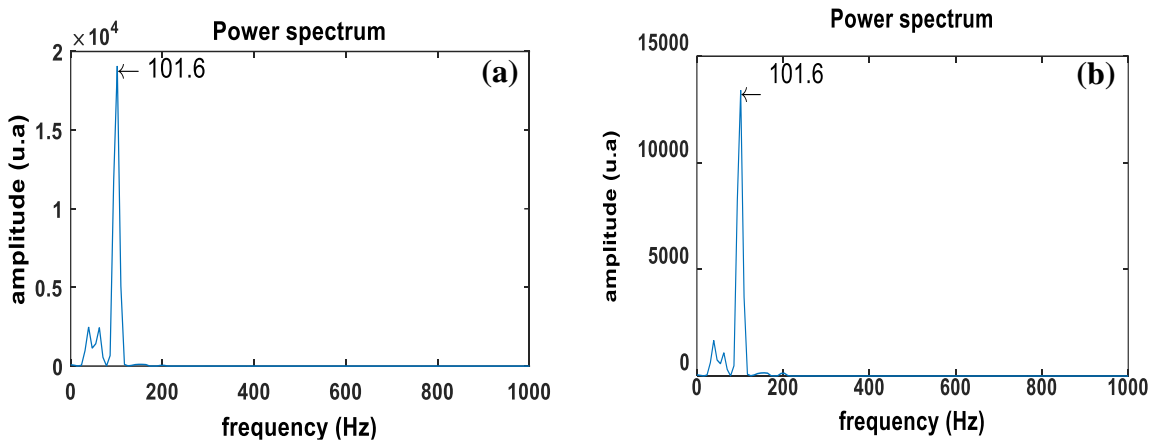


Figure 3.19: The frequency of the magnetic nanoparticles movement for 1% concentration (a) and 0.3% of bare MNPs (b) respectively.

For p6 and p7, the maximum displacements were  $15.55 \pm 0.9$  and  $11.73 \pm 0.56$  μm, respectively, at 50 ms. As can be observed, for low concentration as 0.3 %, the profile of the displacement and the shear wave propagation is maintained.

**The eighth phantom (P8):** The shear wave propagation for this phantom (was included MNPs-100NRL) in two different times is depicted in Figure 3.20. Figure 3.21 shows the value of induced displacement,  $23.41 \pm 1.02$  μm, at 50 ms and the frequency of magnetic nanoparticles displacements (101.6 Hz).

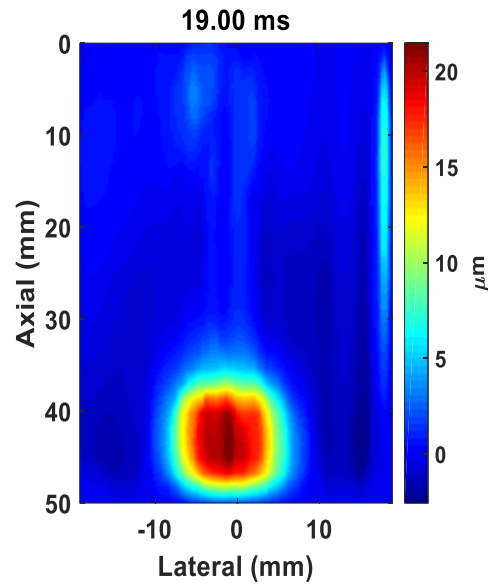


Figure 3.20: Propagation of the shear wave in the phantom eighth with 4% of gelatin and 1 % of MNPs-100NRL (MNPs 5) as an inclusion at 19 ms.

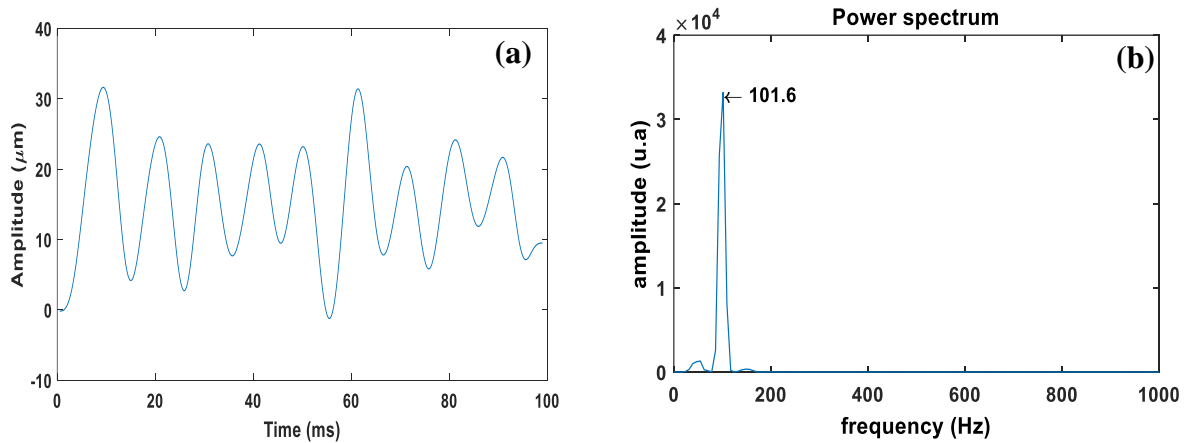


Figure 3.21: Displacements due to the shear wave within the phantom eighth for 4% of gelatin and 1% concentration of MNPs -100NRL (a) and frequency of the magnetic nanoparticles movement (b).

**The ninth phantom(P9):** MNPs-800 NRL (MNPs6) were used as an inclusion, and its results are demonstrated in Figure 3.22-3.23. The induced displacement value was  $23.16 \pm 1.14$  at 50 ms, (Figure 3.24) which is larger than the value for P6 and P7.

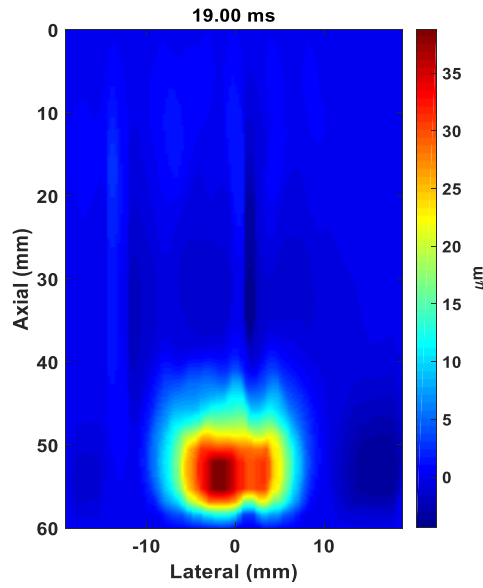


Figure 3.22: Propagation of the shear wave within the gelatin phantom (4%) and 1% of MNPs-NRL800 (MNPs 6) as an inclusion.

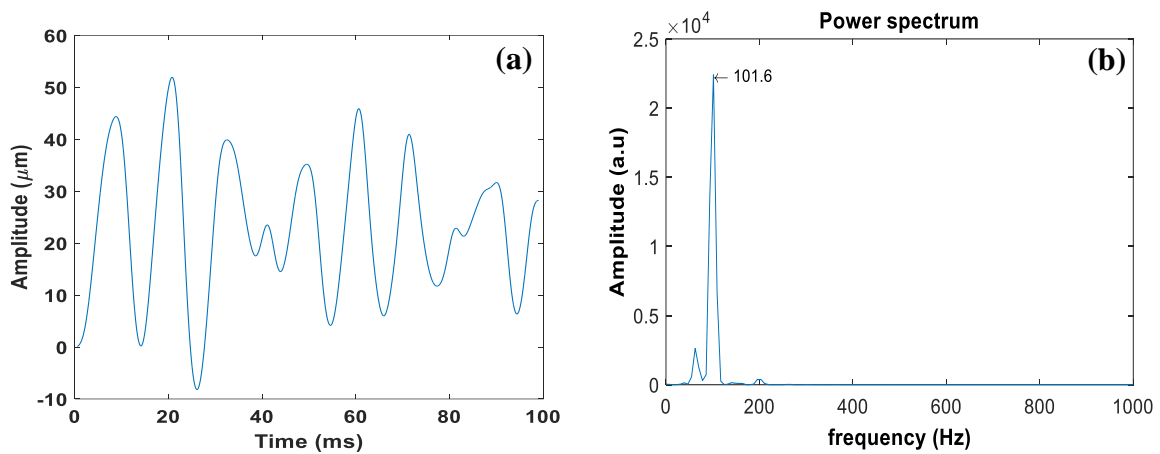


Figure 3.23: Displacement of the shear wave through the gelatin phantom ninth (4%) and 1% concentration of MNPs 800NRL (a) and frequency of the magnetic nanoparticles movement (b).

For the three latter phantoms including MNPs 3, MNPs-100NRL (MNPs 5) and MNPs-800NRL (MNPs 6), different values of velocities were acquired in different frequency, Figure 3.24. Thereafter, the mechanical parameters such as shear elasticity ( $\mu_1$ ) and shear viscosity ( $\mu_2$ ) for these phantoms are reported in the table 3.1.

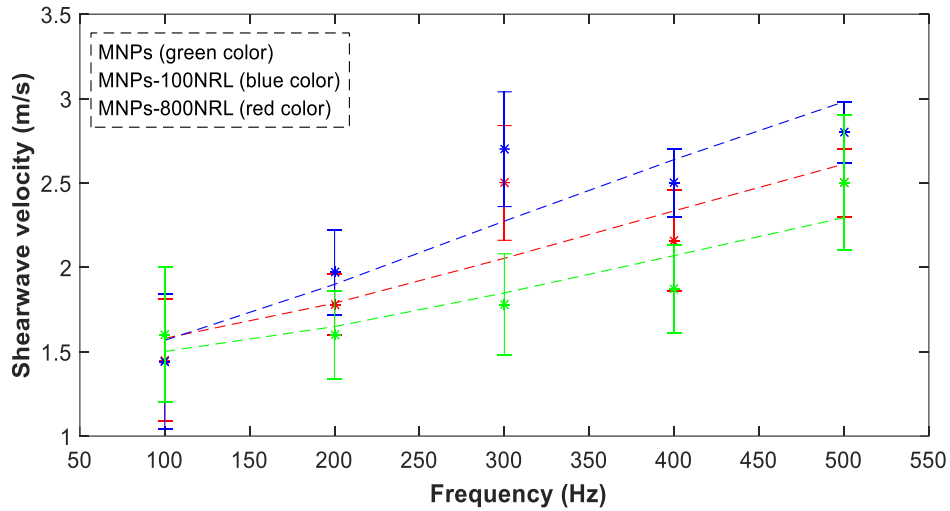


Figure 3.24: Shear wave velocities in a dispersive medium with 4% gelatin for phantoms including bare MNPs, MNPs-100NRL and MNPs-800NRL.

Table 3.1: Mechanical properties of phantoms with 4% gelatin.

	MNPs			MNPs-100NRL			MNPs-800NRL		
$\mu_1$	2.08	$\pm$ 0.37	kPa	2.01	$\pm$ 0.33	kPa	2.23	$\pm$ 0.28	kPa
$\mu_2$	1.08	$\pm$ 0.18	Pa.s	1.78	$\pm$ 0.21	Pa.s	1.4	$\pm$ 0.17	Pa.s

As can be seen in Figure 3.16, the MNPs-800NRL (MNPs6) shows the highest saturation magnetization and thereafter MNPs-100NRL and bare MNPs have lower magnetic saturation, respectively, in the field of 0.16 T. Therefore, as it was expected, MNPs-800 NRL illustrates larger displacements compared to other ones due to the higher magnetization. Based on our results, it can be concluded that the effect of magnetization on the induced displacements is much more pronounced than the size of magnetic nanoparticles.

Finally, according to the results MNPs-800 NRL were selected as the optimized magnetic nanoparticle among those which were used in this thesis. As it was expected, this optimized nanoparticle was the one with the highest magnetization. Figure 3.25 observes the linear relationship between magnetization saturation on the induced displacements of magnetic nanoparticles. Based on the results of all our samples, magnetization of magnetic nanoparticles has a direct influence on the induced displacement.

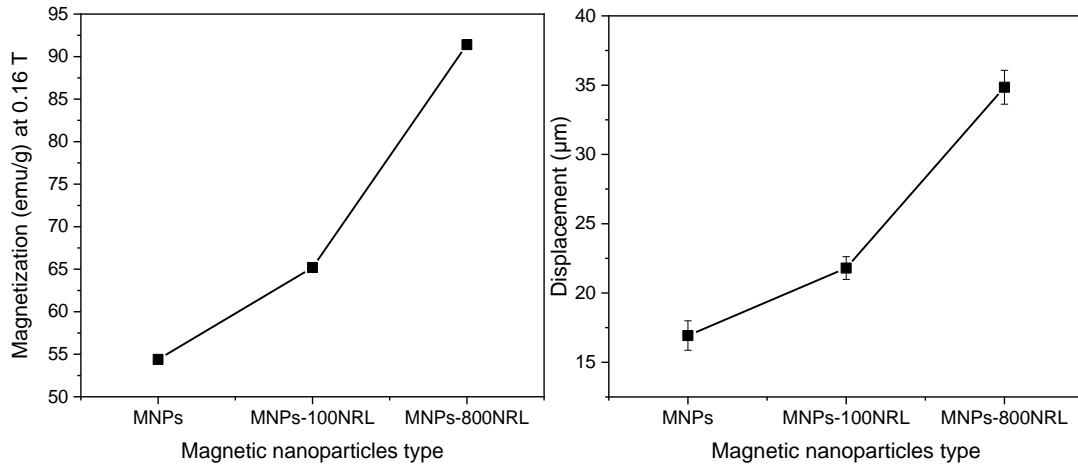


Figure 3.25: The direct relation of magnetization on the induced displacements.

After determining the optimized magnetic nanoparticle, the lowest concentration (0.1%) was used in order to investigate the limitation in SDMMUS modality. Figure 3.26 demonstrates the shear wave propagation through the phantom using 0.2% of concentration. The induced displacement for this phantom was 12.23 μm and also the frequency for magnetic nanoparticles movements (101.6 HZ) are shown in Figure 3.27.

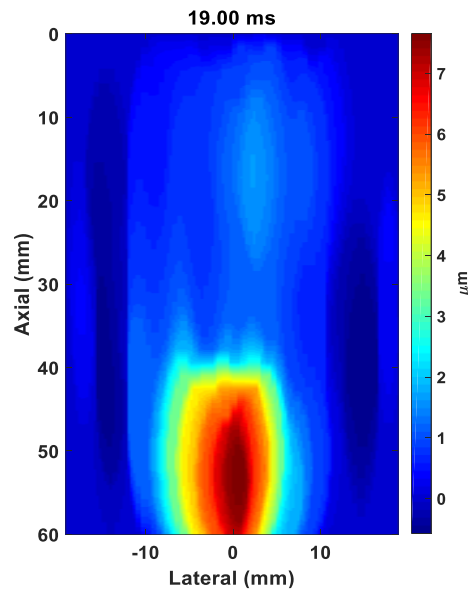


Figure 3.26: The shear wave propagation through the phantom with 0.2% nanoparticle (MNPs-800NRL) as an inclusion in 19 ms.

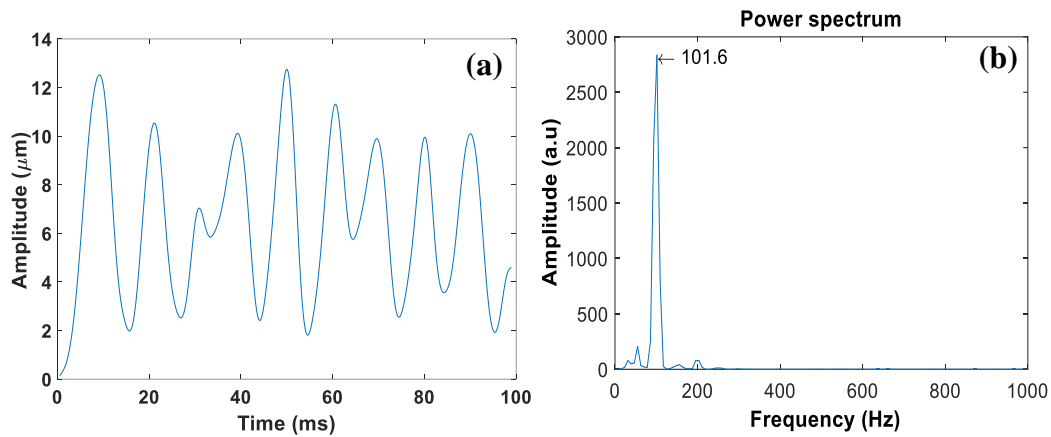


Figure 3.27: Displacements due to the shear wave through the phantom with 0.2 % concentration of MNPs - 800NRL (a) and frequency of the magnetic nanoparticles movement (b).

Finally, four more concentrations (0.1%, 0.2%, 0.3% and 0.7%) were used to confirm the linear relation of the magnetic nanoparticles concentration with the amplitude of the induced displacement. Moreover, a phantom was prepared with an inclusion without any nanoparticles (0.0%) as the control sample to confirm that the observed displacements are due to interaction of the magnetic nanoparticles with the applied field. Clearly, phantoms with higher concentrations exhibit higher motion and there is almost a monotonic increase in the amplitude of displacement by increasing the concentration of nanoparticles (Figure 3.28). The resolution of  $0.31 \mu\text{m}$  was obtained for our system by obtaining the standard deviation.

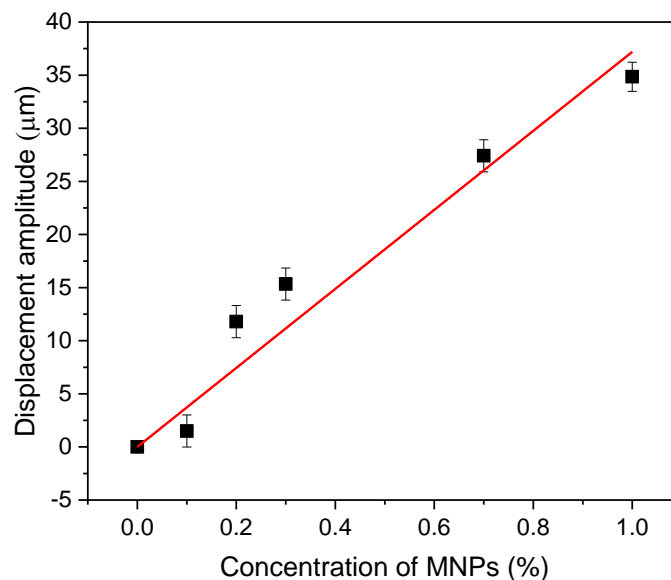


Figure 3.28: The displacement amplitude detected in phantoms with different concentration of MNPs- 800NRL.

Table 3.2: A resume of all used phantoms and physical parameters

<b>Nanoparticles (Fe<sub>3</sub>O<sub>4</sub>)</b>	<b>Size (nm)</b>	<b>Concentration of MNPs (%)</b>	<b>Magnetic saturation (emu/g)</b>	<b>displacement (μm)</b>
<b>MNPs 2</b>	12.5	1	70	20
<b>MNPs 3</b>	20	1	70	20.47
<b>MNPs 4</b>	12±4.1	1	57	15.55
<b>MNPs 4</b>	12±4.1	0.3	85	11.73
<b>MNPs-100NRL (MNPs5)</b>	13±2.8	1	85	23.16
<b>MNPs-800NRL (MNPs6)</b>	7.9±1.5	1	119	34.44
<b>MNPs-800NRL (MNPs6)</b>	7.9±1.5	0.7	119	27.5
<b>MNPs-800NRL (MNPs6)</b>	7.9±1.5	0.3	119	16.35
<b>MNPs-800NRL (MNPs6)</b>	7.9±1.5	0.2	119	12.23
<b>MNPs-800NRL (MNPs6)</b>	7.9±1.5	0.1	119	1.5

It should be mentioned that, the induced displacement in MMUS did not show a uniform pattern during the excitation time for all phantoms except for homogenous ones which have a uniform motions, since these phantoms are more viscous compared to those including inclusion. The main reason for having different values in the displacements' spectrum is due to elastic properties of the medium, where the response is not linear with the waveform of the applied magnetic field. Therefore, the observed displacements are different at various times during the application of the magnetic field.

As it has been shown in previous studies [94, 95] magnetization of magnetic nanoparticles plays a key role in MMUS imaging. This factor was also a significant aspect for SDMMUS experiments in this thesis. Therefore, when applying this technique, it should be noticed that nanoparticles with high magnetization saturation are more appropriate for SDMMU. Using magnetic nanoparticles with high saturation magnetization can result in not only improving the

signal but also reducing the dosage of MNPs which this issue has always been at the center of attention in many studies [110]. The advantages of using lower doses of magnetic nanoparticles can be decreasing the clinical side effects including lower toxicity and damages to cells. Moreover, by enhancing the saturation magnetization of MNPs the cost for generating a high gradient magnetic field will reduce when considering larger volumes, such as in vivo applications.

In this thesis, a low dosage (1%) of MNPs-800NRL with a high saturation magnetization (119 emu/g) and core size of 7.5 nm presented a very satisfactory signal for SDMMUS. However, we showed that even using small doses as 0.2%, it was possible to detect the shear wave with a good signal-to-noise ratio (see figure 3.27). It is the mass percentage of MNPs in a small inclusion (~7 ml) and not in the whole phantom as in the previous study [22, 99]. To explain in more detail, considering the gelatin phantom with the dimensions of  $75 \times 75 \times 75 \text{ mm}^3$  the volume is ~ 422 ml, and 4 wt. % of the nanoparticles will be 20 gr homogeneously dispersed in the whole phantom. Considering in vivo application this mass of nanoparticles is a huge concentration and is not viable. For SDMMUS technique, the region labeled with nanoparticle should be equivalent the area of the magnetization. Whereas, in our case, for a inclusion of 7 ml, 1 wt. % of MNPs correspond to 0.07 g. Comparing these two dosages, the used nanoparticles have been decreased substantially. In addition of using bare MNPs, we also used magnetic nanoparticle with latex covered. Generally, covering is one of the most important parameters in biomedical applications in order to reduce the toxicity and increase the biocompatibility of the surface of MNPs, also it can prevent agglomeration in magnetic nanoparticles. Natural rubber latex (NRL) is not only bioactive, anticancer and biocompatible (Cytotoxicity and anticancer activity of natural rubber latex particles for cancer cells) but also it can increase the magnetization saturation of MNPs. Therefore, this technique (SDMMU) due to the less complexity and being cost effective with acceptable accuracy can be a suitable image modality for detect nanoparticles distribution into biological tissue and as non-contact Rheological technique for *in vivo* viscoelastic evaluation. However, to apply this technique in *in vivo*, more studies are needed.

#### **4. Conclusion**

In this thesis, six magnetic nanoparticles with different properties were used and the effect of magnetization on the displacement and shear wave propagation in gelatin phantom was studied. All the phantoms were consisted of an inclusion prepared with the same materials used

for the phantom plus various percentages of magnetic nanoparticles ( $\text{Fe}_3\text{O}_4$ ) which had different saturation of magnetization. Shear wave were successfully generated for all phantoms and MNPs-800NRL was selected as the optimized one in SDMMUS imaging. It should also mention that the obtained resolution can be estimated  $1.16 \mu\text{m}$  for our system by obtaining the standard deviation of the Figure 3.29. Moreover, by using Voigt model, the mechanical properties of the phantoms were investigated. According to the results, it can be concluded that SDMMUS has a great potential to be used as a remote novel elastography as well as molecular imaging. Meanwhile, by choosing the appropriate magnetic nanoparticles for this diagnostic application, one can consider the potential of the used nanoparticles in theranostics application as well. For example, the same magnetic nanoparticle which is used for imaging might be used in therapeutic application such as magnetic hyperthermia.

## 5. References:

- [1] S. Mallidi *et al.*, “Ultrasound-Based Molecular Imaging Using Nanoagents,” *Nanoplatfrom-Based Molecular Imaging*, pp. 263–278, 2011.
- [2] M. Evertsson *et al.*, “Combined Magnetomotive ultrasound, PET/CT, and MR imaging of <sup>68</sup>Ga-labelled superparamagnetic iron oxide nanoparticles in rat sentinel lymph nodes in vivo,” *Scientific Reports*, vol. 7, no. 1, Dec. 2017.
- [3] A. Cafarelli, A. Verbeni, A. Poliziani, P. Dario, A. Menciassi, and L. Ricotti, “Tuning acoustic and mechanical properties of materials for ultrasound phantoms and smart substrates for cell cultures,” *Acta Biomaterialia*, vol. 49, pp. 368–378, Feb. 2017.
- [4] M. Mahesh, “The Essential Physics of Medical Imaging, Third Edition.,” *Medical Physics*, vol. 40, no. 7, p. 077301, Jun. 2013.
- [5] F. A. Duck, *Physical Properties of Tissues: A Comprehensive Reference Book*. Academic Press, 2013.
- [6] R. S. C. Cobbold, *Foundations of Biomedical Ultrasound*. Oxford University Press, 2007.
- [7] K. K. Shung, *Diagnostic Ultrasound: Imaging and Blood Flow Measurements, Second Edition*. CRC Press, 2015.
- [8] H. Azhari, *Basics of Biomedical Ultrasound for Engineers*. John Wiley & Sons, 2010.
- [9] J. F. V. Vincent, *Structural Biomaterials*. Princeton University Press, 1990.
- [10] Y. C. Fung, *Biomechanics: Motion, Flow, Stress, and Growth*. Springer Science & Business Media, 2013.
- [11] J. Vappou, C. Maleke, and E. E. Konofagou, “Quantitative viscoelastic parameters measured by harmonic motion imaging,” *Physics in Medicine and Biology*, vol. 54, no. 11, pp. 3579–3594, Jun. 2009.
- [12] R. S. Lakes, “Viscoelastic measurement techniques,” *Review of Scientific Instruments*, vol. 75, no. 4, pp. 797–810, Apr. 2004.
- [13] P. N. T. Wells and H.-D. Liang, “Medical ultrasound: imaging of soft tissue strain and elasticity,” *Journal of The Royal Society Interface*, vol. 8, no. 64, pp. 1521–1549, Nov. 2011.
- [14] A. Caenen, “Numerical and Experimental Assessment of Supersonic Shear Wave Imaging as New Non-Invasive Ultrasound Technique for Arterial Stiffness Characterization,” Ghent University, Gent, Belgium, 2013.
- [15] M. Fatemi, A. Manduca, and J. F. Greenleaf, “Imaging elastic properties of biological tissues by low-frequency harmonic vibration,” *Proceedings of the IEEE*, vol. 91, no. 10, pp. 1503–1519, Oct. 2003.
- [16] M. M. Nguyen, S. Zhou, J. Robert, V. Shamdasani, and H. Xie, “Development of Oil-in-Gelatin Phantoms for Viscoelasticity Measurement in Ultrasound Shear Wave Elastography,” *Ultrasound in Medicine & Biology*, vol. 40, no. 1, pp. 168–176, Jan. 2014.
- [17] C. Amador, M. W. Urban, Shigao Chen, Qingshan Chen, Kai-Nan An, and J. F. Greenleaf, “Shear Elastic Modulus Estimation From Indentation and SDUV on Gelatin Phantoms,” *IEEE Transactions on Biomedical Engineering*, vol. 58, no. 6, pp. 1706–1714, Jun. 2011.
- [18] A. Maccabi *et al.*, “Quantitative characterization of viscoelastic behavior in tissue-mimicking phantoms and ex vivo animal tissues,” *PLOS ONE*, vol. 13, no. 1, p. e0191919, Jan. 2018.
- [19] N. Özkaya, D. Leger, D. Goldsheyder, and M. Nordin, “Mechanical Properties of Biological Tissues,” in *Fundamentals of Biomechanics*, Cham: Springer International Publishing, 2017, pp. 361–387.
- [20] T. Deffieux, G. Montaldo, M. Tanter, and M. Fink, “Shear Wave Spectroscopy for In Vivo Quantification of Human Soft Tissues Visco-Elasticity,” *IEEE Transactions on Medical Imaging*, vol. 28, no. 3, pp. 313–322, Mar. 2009.
- [21] A. H. Henni, C. Schmitt, and G. Cloutier, “Shear wave induced resonance elastography of soft heterogeneous media,” *Journal of Biomechanics*, vol. 43, no. 8, pp. 1488–1493, May 2010.
- [22] S. Catheline *et al.*, “Measurement of viscoelastic properties of homogeneous soft solid using transient elastography: An inverse problem approach,” *The Journal of the Acoustical Society of America*, vol. 116, no. 6, pp. 3734–3741, Dec. 2004.
- [23] T. W. J. Almeida, D. R. T. Sampaio, A. C. Bruno, T. Z. Pavan, and A. A. O. Carneiro, “Comparison between shear wave dispersion magneto motive ultrasound and transient elastography for measuring tissue-mimicking phantom viscoelasticity,” *IEEE Transactions on Ultrasonics, Ferroelectrics, and Frequency Control*, vol. 62, no. 12, pp. 2138–2145, Dec. 2015.
- [24] S. Catheline *et al.*, “Measurement of viscoelastic properties of homogeneous soft solid using transient elastography: An inverse problem approach,” *The Journal of the Acoustical Society of America*, vol. 116, no. 6, pp. 3734–3741, 2004.
- [25] Y. Zheng *et al.*, “Shear Wave Propagation in Soft Tissue and Ultrasound Vibrometry,” in *Wave Propagation Theories and Applications*, Y. Zheng, Ed. InTech, 2013.

- [26] H. Zhao, M. Urban, J. Greenleaf, and S. Chen, "Elasticity and viscosity estimation from shear wave velocity and attenuation: A simulation study," in *2010 IEEE International Ultrasonics Symposium*, 2010, pp. 1604–1607.
- [27] V. Egorov, S. Tsyuryupa, S. Kanilo, M. Kogit, and A. Sarvazyan, "Soft tissue elastometer," *Medical Engineering & Physics*, vol. 30, no. 2, pp. 206–212, Mar. 2008.
- [28] Y. Wang, "Soft tissue viscoelastic properties: measurements, models and interpretation," 2016.
- [29] "Elasticity and viscosity estimation from shear wave velocity and attenuation: A simulation study - IEEE Conference Publication." [Online]. Available: <https://ieeexplore.ieee.org/document/5935462/>. [Accessed: 14-Jun-2018].
- [30] S. Chen *et al.*, "Shearwave dispersion ultrasound vibrometry (SDUV) for measuring tissue elasticity and viscosity," *IEEE Transactions on Ultrasonics, Ferroelectrics, and Frequency Control*, vol. 56, no. 1, pp. 55–62, Jan. 2009.
- [31] S. Chen, M. Fatemi, and J. F. Greenleaf, "Quantifying elasticity and viscosity from measurement of shear wave speed dispersion," *J. Acoust. Soc. Am.*, vol. 115, no. 6, pp. 2781–2785, Jun. 2004.
- [32] J. Ophir, "Elastography: A quantitative method for imaging the elasticity of biological tissues," *Ultrasonic Imaging*, vol. 13, no. 2, pp. 111–134, Apr. 1991.
- [33] M. Fatemi and J. F. Greenleaf, "Imaging the Viscoelastic Properties of Tissue," in *Imaging of Complex Media with Acoustic and Seismic Waves*, Springer, Berlin, Heidelberg, 2002, pp. 257–276.
- [34] Y. K. Mariappan, K. J. Glaser, and R. L. Ehman, "Magnetic resonance elastography: A review," *Clinical Anatomy*, vol. 23, no. 5, pp. 497–511, Jun. 2010.
- [35] J. F. Greenleaf, M. Fatemi, and M. Insana, "Selected Methods for Imaging Elastic Properties of Biological Tissues," *Annual Review of Biomedical Engineering*, vol. 5, no. 1, pp. 57–78, Aug. 2003.
- [36] A. S. Khalil, R. C. Chan, A. H. Chau, B. E. Bouma, and M. R. K. Mofrad, "Tissue Elasticity Estimation with Optical Coherence Elastography: Toward Mechanical Characterization of <Emphasis Type="Italic">In Vivo</Emphasis> Soft Tissue," *Ann Biomed Eng*, vol. 33, no. 11, pp. 1631–1639, Nov. 2005.
- [37] V. Garge, K. Waikul, and V. J. Kadam, "Elastography: Techniques and Applications," pp. 359–368, 2015.
- [38] U. Zaleska-Dorobisz, K. Kaczorowski, A. Pawluś, A. Puchalska, and M. Ingot, "Ultrasound elastography - review of techniques and its clinical applications," *Adv Clin Exp Med*, vol. 23, no. 4, pp. 645–655, Aug. 2014.
- [39] L. Gao, K. J. Parker, S. K. Alam, and R. M. Lerner, "Sonoelasticity imaging: theory and experimental verification," *J. Acoust. Soc. Am.*, vol. 97, no. 6, pp. 3875–3886, Jun. 1995.
- [40] J. Bercoff, M. Tanter, and M. Fink, "Supersonic shear imaging: a new technique for soft tissue elasticity mapping," *IEEE Transactions on Ultrasonics, Ferroelectrics and Frequency Control*, vol. 51, no. 4, pp. 396–409, Apr. 2004.
- [41] K. Nightingale, "Acoustic Radiation Force Impulse (ARFI) Imaging: a Review," *Curr Med Imaging Rev*, vol. 7, no. 4, pp. 328–339, Nov. 2011.
- [42] A. P. Sarvazyan, O. V. Rudenko, S. D. Swanson, J. B. Fowlkes, and S. Y. Emelianov, "Shear wave elasticity imaging: a new ultrasonic technology of medical diagnostics," *Ultrasound in Medicine & Biology*, vol. 24, no. 9, pp. 1419–1435, Dec. 1998.
- [43] S. MCALEAVEY, E. COLLINS, J. KELLY, E. ELEGBE, and M. MENON, "VALIDATION OF SMURF ESTIMATION OF SHEAR MODULUS IN HYDROGELS," *Ultrason Imaging*, vol. 31, no. 2, pp. 131–150, Apr. 2009.
- [44] R. M. Lerner, S. R. Huang, and K. J. Parker, "'Sonoelasticity' images derived from ultrasound signals in mechanically vibrated tissues," *Ultrasound in Medicine & Biology*, vol. 16, no. 3, pp. 231–239, Jan. 1990.
- [45] Z. Wu, L. S. Taylor, D. J. Rubens, and K. J. Parker, "Sonoelastographic imaging of interference patterns for estimation of the shear velocity of homogeneous biomaterials," *Physics in Medicine and Biology*, vol. 49, no. 6, pp. 911–922, Mar. 2004.
- [46] M. H. Wang, "Shear wave imaging using acoustic radiation force," 2013.
- [47] C. A. Carrascal, "Measurement of kidney viscoelasticity with shearwave dispersion ultrasound vibrometry," 2011.
- [48] D. V. Litwiller, Y. K. Mariappan, and R. L. Ehman, "Magnetic Resonance Elastography," *Curr Med Imaging Rev*, vol. 8, no. 1, pp. 46–55, 2012.
- [49] D. Klatt, C. Friedrich, Y. Korth, R. Vogt, J. Braun, and I. Sack, "Viscoelastic properties of liver measured by oscillatory rheometry and multifrequency magnetic resonance elastography," *Biorheology*, vol. 47, no. 2, pp. 133–141, Jan. 2010.
- [50] J. R. A. Loureiro, "Magnetic resonance elastography: design and implementation as a clinical tool," 2012.
- [51] E. Park and A. M. Maniatty, "Shear modulus reconstruction in dynamic elastography: time harmonic case," *Phys. Med. Biol.*, vol. 51, no. 15, p. 3697, 2006.
- [52] A. Sarvazyan, "A new approach to remote ultrasonic evaluation of viscoelastic properties of tissues for diagnostics and healing monitoring," presented at the Abstract of ARPA/ONR Medical Ultrasonic Imaging Technology Workshop, Landsdowne, Virginia, 1995, pp. 24–26.

- [53] C. Vorländer, J. Wolff, S. Saalabian, R. H. Lienenlücke, and R. A. Wahl, “Real-time ultrasound elastography—a noninvasive diagnostic procedure for evaluating dominant thyroid nodules,” *Langenbeck’s archives of surgery*, vol. 395, no. 7, pp. 865–871, 2010.
- [54] L. Sandrin *et al.*, “Transient elastography: a new noninvasive method for assessment of hepatic fibrosis,” *Ultrasound in medicine & biology*, vol. 29, no. 12, pp. 1705–1713, 2003.
- [55] M. Friedrich–Rust *et al.*, “Performance of transient elastography for the staging of liver fibrosis: a meta-analysis,” *Gastroenterology*, vol. 134, no. 4, pp. 960–974, 2008.
- [56] G. D. Kirk *et al.*, “Assessment of liver fibrosis by transient elastography in persons with hepatitis C virus infection or HIV–hepatitis C virus coinfection,” *Clinical Infectious Diseases*, vol. 48, no. 7, pp. 963–972, 2009.
- [57] M. O. Culjat, D. Goldenberg, P. Tewari, and R. S. Singh, “A review of tissue substitutes for ultrasound imaging,” *Ultrasound in medicine & biology*, vol. 36, no. 6, pp. 861–873, 2010.
- [58] E. L. Madsen, J. A. Zagzebski, R. A. Banjavie, and R. E. Jutila, “Tissue mimicking materials for ultrasound phantoms,” *Medical physics*, vol. 5, no. 5, pp. 391–394, 1978.
- [59] T. J. Hall, M. Bilgen, M. F. Insana, and T. A. Krouskop, “Phantom materials for elastography,” *IEEE transactions on ultrasonics, ferroelectrics, and frequency control*, vol. 44, no. 6, pp. 1355–1365, 1997.
- [60] K. Kawabata, Y. Waki, T. Matsumura, and S. Umemura, “Tissue mimicking phantom for ultrasonic elastography with finely adjustable elastic and echographic properties,” presented at the Ultrasonics Symposium, 2004 IEEE, 2004, vol. 2, pp. 1502–1505.
- [61] T. Ling, Q. Jin, H. Yao, and H. Zheng, “Design and Characterization of a Tissue-Mimicking Phantom for Ultrasonic Elastography,” in *2010 4th International Conference on Bioinformatics and Biomedical Engineering*, 2010, pp. 1–4.
- [62] K. Zell, J. Sperl, M. Vogel, R. Niessner, and C. Haisch, “Acoustical properties of selected tissue phantom materials for ultrasound imaging,” *Physics in Medicine & Biology*, vol. 52, no. 20, p. N475, 2007.
- [63] M. H. Han, “Development of synthesis method for spinel ferrite magnetic nanoparticle and its superparamagnetic properties,” Aug. 2008.
- [64] R. C. O’Handley, *Modern Magnetic Materials: Principles and Applications*. Wiley, 1999.
- [65] B. D. Cullity and C. D. Graham, *Introduction to Magnetic Materials*. Wiley, 2011.
- [66] C. Xu and S. Sun, “Superparamagnetic nanoparticles as targeted probes for diagnostic and therapeutic applications,” *Dalton Trans.*, vol. 0, no. 29, pp. 5583–5591, Jul. 2009.
- [67] “Magnetic nanoparticles for the manipulation of proteins and cells. - Semantic Scholar.” [Online]. Available: /paper/Magnetic-nanoparticles-for-the-manipulation-of-and-Pan-Du/3fbb2da19d76c7b7d94299f1f52617616feb5b34. [Accessed: 20-Jul-2018].
- [68] I. M. Obaidat, B. Issa, and Y. Haik, “Magnetic Properties of Magnetic Nanoparticles for Efficient Hyperthermia,” *Nanomaterials*, vol. 5, no. 1, pp. 63–89, Jan. 2015.
- [69] J. Ding, K. Tao, J. Li, S. Song, and K. Sun, “Cell-specific cytotoxicity of dextran-stabilized magnetite nanoparticles,” *Colloids and Surfaces B: Biointerfaces*, vol. 79, no. 1, pp. 184–190, 2010.
- [70] C. Xu and S. Sun, “New forms of superparamagnetic nanoparticles for biomedical applications,” *Advanced Drug Delivery Reviews*, vol. 65, no. 5, pp. 732–743, May 2013.
- [71] F. Gaboriaud, B. de Gaudemaris, T. Rousseau, S. Derclaye, and Y. F. Dufrêne, “Unravelling the nanometre-scale stimuli-responsive properties of natural rubber latex particles using atomic force microscopy,” *Soft Matter*, vol. 8, no. 9, pp. 2724–2729, 2012.
- [72] Q. Pankhurst, N. Thanh, S. Jones, and J. Dobson, “Progress in applications of magnetic nanoparticles in biomedicine,” *Journal of Physics D: Applied Physics*, vol. 42, no. 22, p. 224001, 2009.
- [73] J. Oh, M. D. Feldman, J. Kim, C. Condit, S. Emelianov, and T. E. Milner, “Detection of magnetic nanoparticles in tissue using magneto-motive ultrasound,” *Nanotechnology*, vol. 17, no. 16, p. 4183, 2006.
- [74] V. Silva, P. Andrade, M. Silva, L. D. L. S. Valladares, and J. A. Aguiar, “Synthesis and characterization of Fe<sub>3</sub>O<sub>4</sub> nanoparticles coated with fucan polysaccharides,” *Journal of Magnetism and Magnetic Materials*, vol. 343, pp. 138–143, 2013.
- [75] M. Mozaffari, Y. Hadadian, A. Aftabi, and M. O. Moakhar, “The effect of cobalt substitution on magnetic hardening of magnetite,” *Journal of Magnetism and Magnetic Materials*, vol. 354, pp. 119–124, 2014.
- [76] J. L. Arias, M. López-Viota, M. A. Ruiz, J. López-Viota, and A. V. Delgado, “Development of carbonyl iron/ethylcellulose core/shell nanoparticles for biomedical applications,” *International Journal of Pharmaceutics*, vol. 339, no. 1, pp. 237–245, Jul. 2007.
- [77] J. Chomoucka, J. Drbohlavova, D. Huska, V. Adam, R. Kizek, and J. Hubalek, “Magnetic nanoparticles and targeted drug delivering,” *Pharmacological Research*, vol. 62, no. 2, pp. 144–149, 2010.
- [78] S. Dutz *et al.*, “Influence of dextran coating on the magnetic behaviour of iron oxide nanoparticles,” *Journal of Magnetism and Magnetic Materials*, vol. 311, no. 1, pp. 51–54, 2007.
- [79] A. Kumari, V. Kumar, and S. K. Yadav, “Plant extract synthesized PLA nanoparticles for controlled and sustained release of quercetin: a green approach,” *PLoS One*, vol. 7, no. 7, p. e41230, 2012.

- [80] E. J. Guidelli, A. P. Ramos, M. E. D. Zaniquelli, and O. Baffa, "Green synthesis of colloidal silver nanoparticles using natural rubber latex extracted from *Hevea brasiliensis*," *Spectrochimica Acta Part A: Molecular and Biomolecular Spectroscopy*, vol. 82, no. 1, pp. 140–145, 2011.
- [81] N. A. Kalkan, S. Aksoy, E. A. Aksoy, and N. Hasirci, "Preparation of chitosan-coated magnetite nanoparticles and application for immobilization of laccase," *Journal of Applied Polymer Science*, vol. 123, no. 2, pp. 707–716, 2012.
- [82] M. Mehrmohammadi, "Pulsed magneto-motive ultrasound imaging," May 2012.
- [83] J. U. Voigt, "Ultrasound molecular imaging.," *Methods*, vol. 48, no. 2, pp. 92–97, Jun. 2009.
- [84] I. Brigger, C. Dubernet, and P. Couvreur, "Nanoparticles in cancer therapy and diagnosis," *Advanced drug delivery reviews*, vol. 64, pp. 24–36, 2012.
- [85] R. Weissleder, "Molecular imaging in cancer," *Science*, vol. 312, no. 5777, pp. 1168–1171, 2006.
- [86] R. Weissleder and U. Mahmood, "Molecular imaging," *Radiology*, vol. 219, no. 2, pp. 316–333, 2001.
- [87] A. Webb and G. C. Kagadis, "Introduction to biomedical imaging," *Medical Physics*, vol. 30, no. 8, pp. 2267–2267, 2003.
- [88] M. Mehrmohammadi, J. Oh, S. Mallidi, and S. Y. Emelianov, "Pulsed Magneto-motive Ultrasound Imaging Using Ultrasmall Magnetic Nanoprobos," *Mol Imaging*, vol. 10, no. 2, pp. 102–110, Apr. 2011.
- [89] J. F. Schenck, "The role of magnetic susceptibility in magnetic resonance imaging: MRI magnetic compatibility of the first and second kinds," *Medical physics*, vol. 23, no. 6, pp. 815–850, 1996.
- [90] M. Mehrmohammadi, K. Yoon, M. Qu, K. Johnston, and S. Emelianov, "Enhanced pulsed magneto-motive ultrasound imaging using superparamagnetic nanoclusters," *Nanotechnology*, vol. 22, no. 4, p. 045502, 2010.
- [91] M. Evertsson, "Development of Magnetomotive Ultrasound Imaging," Lund University, 2016.
- [92] M. Mehrmohammadi *et al.*, "Imaging of iron oxide nanoparticles using magneto-motive ultrasound," in *2007 IEEE Ultrasonics Symposium Proceedings, IUS*, 2007, pp. 652–655.
- [93] M. Mehrmohammadi, J. Oh, S. R. Aglyamov, A. B. Karpiouk, and S. Y. Emelianov, "Pulsed magneto-acoustic imaging," presented at the Engineering in Medicine and Biology Society, 2009. EMBC 2009. Annual International Conference of the IEEE, 2009, pp. 4771–4774.
- [94] M. Mehrmohammadi *et al.*, "In vivo pulsed magneto-motive ultrasound imaging using high-performance magnetoactive contrast nanoagents," *Nanoscale*, vol. 5, no. 22, pp. 11179–11186, 2013.
- [95] Y. Hadadian *et al.*, "Synthesis and characterization of zinc substituted magnetite nanoparticles and their application to magneto-motive ultrasound imaging," *Journal of Magnetism and Magnetic Materials*, vol. 465, pp. 33–43, Nov. 2018.
- [96] C. Wei *et al.*, "Magnetomotive photoacoustic imaging: in vitro studies of magnetic trapping with simultaneous photoacoustic detection of rare circulating tumor cells," *Journal of Biophotonics*, vol. 6, no. 6–7, pp. 513–522.
- [97] A. C. Bruno, O. Baffa, and A. O. Carneiro, "Hybrid system for magnetic and acoustic measurement," *Conf Proc IEEE Eng Med Biol Soc*, vol. 2009, pp. 761–764, 2009.
- [98] M. Evertsson *et al.*, "Multimodal detection of iron oxide nanoparticles in rat lymph nodes using magnetomotive ultrasound imaging and magnetic resonance imaging," *IEEE Transactions on Ultrasonics, Ferroelectrics, and Frequency Control*, vol. 61, no. 8, pp. 1276–1283, Aug. 2014.
- [99] T. W. J. de Almeida, "Sistema para análise viscoelástica de tecidos moles por ondas de cisalhamento usando excitação magnética e medida ultrassônica," text, Universidade de São Paulo, 2015.
- [100] S. Bernard, S. Kazemirad, and G. Cloutier, "A Frequency-Shift Method to Measure Shear-Wave Attenuation in Soft Tissues," *IEEE Transactions on Ultrasonics, Ferroelectrics, and Frequency Control*, vol. 64, no. 3, pp. 514–524, Mar. 2017.
- [101] Diego R. Thomaz, "Implementação da técnica de magneto-acustografia em um equipamento de ultrassom diagnóstico..."
- [102] "Sistema para análise viscoelástica de tecidos moles por ondas de cisalhamento usando..." [Online]. Available: <http://www.teses.usp.br/teses/disponiveis/59/59135/tde-28052015-172233/pt-br.php>. [Accessed: 14-Jun-2018].
- [103] "Nonlinear elastic behavior of phantom materials for elastography - IOPscience." [Online]. Available: <http://iopscience.iop.org/article/10.1088/0031-9155/55/9/017/meta>. [Accessed: 14-Jun-2018].
- [104] "Phantom materials for elastography - IEEE Journals & Magazine." [Online]. Available: <https://ieeexplore.ieee.org/document/656639/>. [Accessed: 14-Jun-2018].
- [105] S. Chen, M. Fatemi, and J. F. Greenleaf, "Quantifying elasticity and viscosity from measurement of shear wave speed dispersion," *The Journal of the Acoustical Society of America*, vol. 115, no. 6, pp. 2781–2785, Jun. 2004.
- [106] "An Algorithm for Least-Squares Estimation of Nonlinear Parameters | Journal of the Society for Industrial and Applied Mathematics | Vol. 11, No. 2 | Society for Industrial and Applied Mathematics." [Online]. Available: <https://epubs.siam.org/doi/abs/10.1137/0111030>. [Accessed: 14-Jun-2018].

- [107] T. W. J. de Almeida, “Sistema para análise viscoelástica de tecidos moles por ondas de cisalhamento usando excitação magnética e medida ultrassônica,” text, Universidade de São Paulo, 2015.
- [108] “Comparison between shear wave dispersion magneto motive ultrasound and transient elastography for measuring tissue-mimicking phantom viscoelasticity. - PubMed - NCBI.” [Online]. Available: <https://www.ncbi.nlm.nih.gov/pubmed/26670853>. [Accessed: 20-Jun-2018].
- [109] Y. Zheng *et al.*, “Shear Wave Propagation in Soft Tissue and Ultrasound Vibrometry,” in *Wave Propagation Theories and Applications*, Y. Zheng, Ed. InTech, 2013.
- [110] R. Banerjee, Y. Katsenovich, L. Lagos, M. McIntosh, X. Zhang, and C.-Z. Li, “Nanomedicine: Magnetic Nanoparticles and their Biomedical Applications,” *Current Medicinal Chemistry*, vol. 17, no. 27, pp. 3120–3141, Sep. 2010.